**Lehrstuhl für
Technische Dynamik**

Prof. Dr.-Ing. habil. Sigrid Leyendecker

Report
Chair of Applied Dynamics
January 2014 – December 2014

FAU

**FRIEDRICH-ALEXANDER
UNIVERSITÄT
ERLANGEN-NÜRNBERG**

TECHNISCHE FAKULTÄT

Contents

1 Preface

This report summarises the activities in research and teaching of the Chair of Applied Dynamics at the University of Erlangen-Nuremberg between January and December 2014.

Part of LTD is the Independent Junior Research Group in the DFG Emmy Noether Programme 'Simulation and optimal control of the dynamics of multibody systems in biomechanics and robotics' that has been at the University of Kaiserslautern from May 2009 to March 2011. Research topics are situated in the field of computational mechanics, in particular dynamics and applied mathematics with focus on the simulation of human motion (everyday movements and sports) and robot dynamics as well as the optimisation and optimal control of their dynamics. Further topics are the modelling and simulation of artificial muscles as electromechanically coupled problems, multirate systems with dynamics on various time scales, Lie group methods and viscous beam formulations.

2 Team

chair holder
Prof. Dr.-Ing. habil. Sigrid Leyendecker

technical staff
Beate Hegen
Dipl.-Ing. (FH) Natalia Kondratieva
Sven Lässig

academic scientist
Dr. rer. nat. Holger Lang

postdoc
Dr. Odysseas T. Kosmas

scientific staff

M.Sc. Dominik Budday	since 01.06.2014
Dipl.-Ing. Nathanael Bach	
Dipl.-Ing. Tobias Gail	
Dipl.-Ing. Michael W. Koch	until 31.08.2014
Dipl.-Ing. Thomas Leitz	
Dipl.-Math. Maik Ringkamp	
Dipl.-Ing. Tristan Schlögl	

students

|	
Theresa Ach	Tobias Bader
Dominik Bartels	Larissa Bugert
Emre Cicek	Selcuk Demirel
Roman Enser	Andreas Enzenhöfer
Christian Feuerer	Gurloss Habuer
Johannes Henneberg	Michael Jäger
Dominik Kalb	Simone Kellermann
Johannes Koch	Julius Kohnert
Jonas Koppmann	Hannah Laube
Antonia Lion	Roland Purucker
Rene Rathmann	Dominik Reichl
Riedel Sebastian	Judith Saffer
Sebastian Scheiterer	Cosima Schellenberger
Selina Scherzer	Simon Schindler
Christian Sperber	Johannes Vorndran
Thomas Will	Theresa Wenger
Faisal Yassin	Johannes Zapf
Daniel Zint	Natalie Zipf

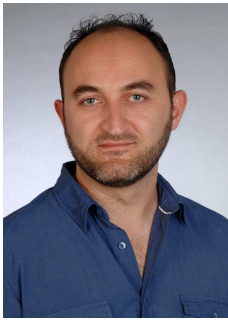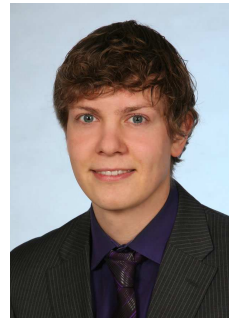B. Hegen

N. Kondratieva
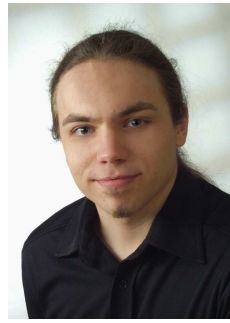
S. Lässig
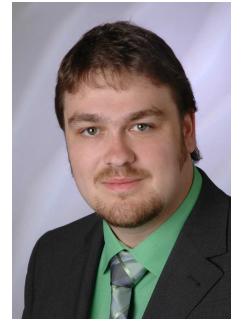

H. Lang

O.T. Kosmas

N. Bach

D. Budday

T. Gail

M.W. Koch

T. Leitz

M. Ringkamp

T. Schlögl

S. Leyendecker

3 Research

3.1 Emmy Noether Independent Junior Research Group

The Emmy Noether Programme by the German Research Foundation (DFG) supports young researchers in achieving independence at an early stage of their scientific careers. Between May 2009 and March 2011, the Emmy Noether Independent Junior Research Group 'Simulation and optimal control of the dynamics of multibody systems in biomechanics and robotics' has been affiliated with the University of Kaiserslautern. The group has been transferred to the University of Erlangen-Nuremberg in April 2011 being now part of the Chair of Applied Dynamics.

3.2 Bionicum

The Bavarian Environment Agency (LfU) (being the central authority for environmental protection and nature conservation, geology and water resources management) has established the centre for bionics 'bionicum' in 2012, consisting of a visitors centre in the Tiergarten of the City of Nuremberg with a permanent exhibition and three research projects with a total financial volume of eight million Euro. One of the projects investigates artificial muscles. The modelling and simulation of the dielectric elastomer actors is developed at the LTD while the Institute for Factory Automation and Production Systems (FAPS) works on the fabrication.

3.3 BaCaTeC

The Bavaria California Technology Center at the University of Erlangen-Nuremberg supports newly initiated cooperations between researchers from Bavaria and California. From July 2014 on, BaCaTeC sponsors the LTD for the established collaboration with the Stanford Synchrotron Radiation Lightsource (SSRL) on 'Inferring rigid substructures in proteins from X-ray data using the null space topology'.

3.4 Cooperation partners

Besides numerous worldwide cooperations with scientists in academia, the LTD is in contact with other institutions and industrial partners. The LTD cooperates with the Fraunhofer Institute for Industrial and Economical Mathematics (ITWM) in Kaiserslautern on common interests like biomechanics and nonlinear rod dynamics for wind turbine rotor blades. A recently started cooperation with the German Research Center for Artificial Intelligence (DFKI), aims at bridging the gap between motion capturing and biomechanical optimal control simulations. In collaboration with the Stanford Synchrotron Radiation Lightsource (SSRL), the LTD does research on structural rigidity and conformational analysis of biomolecules.

3.5 GAMM and GACM

Sigrid Leyendecker has been elected as an Executive Council Members of the German Association for Computational Mechanics (GACM) for the period of January 2013 to December 2016. The objective of GACM is to stimulate and promote education, research and practice in computational mechanics and computational methods in applied sciences, to foster the interchange of ideas among various fields contributing to computational mechanics, and to provide forums and meetings for the dissemination of knowledge about computational mechanics in Germany.

In February 2014, she has further been elected as a member of the Managing Board of the International Association of Applied Mathematics and Mechanics (GAMM) for two years. GAMM promotes scientific development in all areas of applied mathematics and mechanics, e.g. via the organisation of

workshops, in particular for younger scientists, and the international scientific annual GAMM meeting, taking place in Erlangen in March 2014.

3.6 Scientific reports

The following pages present a short overview on ongoing research projects pursued at the Chair of Applied Dynamics. These are partly financed by third-party funding (German Research Foundation (DFG), Bavarian Environment Agency (LfU)) and in addition by the core support of the university.

Research topics

Various multibody dynamic models for the description of plane Kirchhoff rods
Holger Lang, Hannah Laube, Sigrid Leyendecker

Exponential variational integrators for split potential systems
Odysseas Kosmas, Sigrid Leyendecker

Characterizing rigidity in biomolecules with geometric tools
Dominik Budday, Sigrid Leyendecker, Henry van den Bedem

On the role of quadrature rules and system dimensions in variational multirate integrators
Tobias Gail, Sina Ober-Blöbaum, Sigrid Leyendecker

Structure preserving optimal control of a 3d-dimensional upright gait
Michael W. Koch, Sigrid Leyendecker

Various quadrature rules for the approximation of the action integral in non-linear beam dynamics and elastostatics
Thomas Leitz, Sigrid Leyendecker

Relaxing mixed integer optimal control problems using a time transformation
Maik Ringkamp, Sina Ober-Blöbaum, Sigrid Leyendecker

Viscoelastic finite element modelling of dielectric elastomers
Tristan Schlögl, Sigrid Leyendecker

Various multibody dynamic models for the description of plane Kirchhoff rods

Holger Lang, Hannah Laube, Sigrid Leyendecker

The plane Kirchhoff rod model is well known in continuum mechanics for the dynamic simulation of slender structures. It is a geometrically exact generalisation of the linear Euler-Bernoulli beam that takes into account the effect of extensional and bending deformations. In contrast to a Reissner rod, the rigid cross sections always stay perpendicular to the centerline of mass centroids. Therefore, it does not incorporate transverse shear and it is well suited for very slim structures.
We consider a Finite Element discretisation that is based on the discrete Kirchhoff beam kinematics displayed in Figure 1. It is a 2D restriction of the one proposed in [2] for 3D Kirchhoff and Cosserat rods on a staggered grid. The proper choice of coordinates plays a crucial role concerning accuracy

and numerical complexity during time integration. Here, we compare three approaches, which are well known in multibody dynamics simulations, and apply them to the proposed FE model.
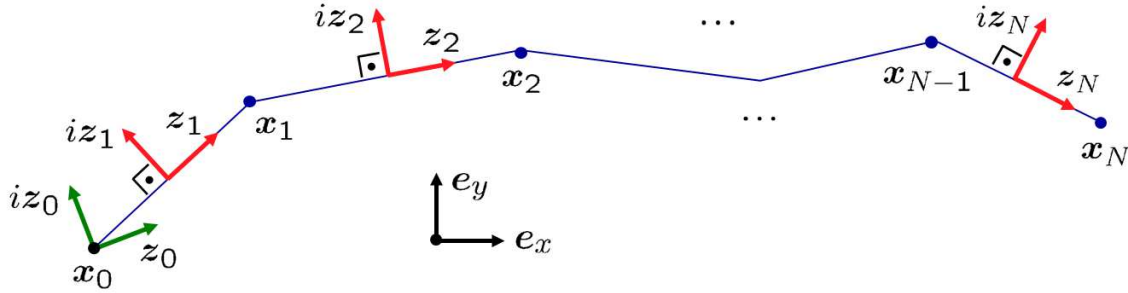

Figure 1: Plane Kirchhoff beam kinematics. The directors z_n resp. iz_n are parallel resp. orthogonal to the discrete centerline tangents $x_n - x_{n-1}$. The director iz_n indicates the orientation of the rigid cross section. x_0 and z_0 are prescribed as boundary values.

First approach It uses *redundant absolute coordinates* $p = (z_1, x_1, \ldots, z_N, x_N)$, where the $x_n \in \mathbb{R}^2$ stand for the absolute translations (the cross section centroid positions) and $z_n \in \mathbb{S}^1 = \{z \in \mathbb{C} : \|z\|^2 = 1\} \simeq SO(2)$ for the absolute rotations (the cross section orientations). The shear rigidity and the unity conditions for z_n lead to internal holonomic constraints of the form $g(p) = 0$ with the d'Alembert constraint forces $G(p)^\top \lambda$, where $G(p) = \nabla g(p)$. The standard index 1 version of the equations of motion takes the form

$$\left[\begin{array}{c} \ddot{p} \\ \lambda \end{array} \right] = \left[\begin{array}{cc} M(p) & G(p)^\top \\ G(p) & 0 \end{array} \right]^{-1} \left[\begin{array}{c} f(p, \dot{p}, t) \\ -\dot{G}(p, \dot{p})\dot{p} \end{array} \right] \tag{1}$$

with a state dependent mass $M(p)$ and $f(p, \dot{p}, t)$ incorporating the internal and external forces and moments. Due to the parametrisation of rotations by complex numbers, f is free of trigonometric expressions and therefore fast to evaluate. Solving the linear system of equation in each time step grows with complexity $\mathcal{O}(N)$, as the structure is block-banded [3]. See Figure 2 on the left.

Second approach It uses *minimal relative (or 'joint') coordinates* $q = (w_1, \xi_1, \ldots, w_N, \xi_N)$. Here, we let

$$\xi_n = \|x_n - x_{n-1}\| \qquad \text{resp.} \qquad w_n = \Im(\bar{z}_{n-1} z_n) \qquad \text{for} \quad n = 1, \ldots, N \tag{2}$$

for the relative translations resp. relative rotations. In the context of continuum mechanics, the magnitudes ξ_n correspond to the *extensional strains*, the w_n to the *bending curvatures*. This means that the *strains* are used as the primary unknowns instead of the displacements, which is not standard in continuum mechanics. We write $q = \psi(p)$ to denote the forward recursion (2), transferring the absolute to the relative coordinates. Its inverse, the backward recursive transformation $p = \varphi(q)$, is given by

$$x_n = x_{n-1} + \xi_n z_n \qquad \text{resp.} \qquad z_n = \left(\sqrt{1 - w_n^2} + i w_n \right) z_{n-1} \qquad \text{for} \quad n = 1, \ldots, N. \tag{3}$$

System (1) is then transformed to the equivalent form

$$\mathcal{M}(q)\ddot{q} \;=\; \Phi(q)^\top \big\{ f(p, \dot{p}, t) - M(p)\dot{\Phi}(q, \dot{q})\dot{q} \big\} \Big|_{p=\varphi(q), \, \dot{p}=\Phi(q)\dot{q}} \tag{4}$$
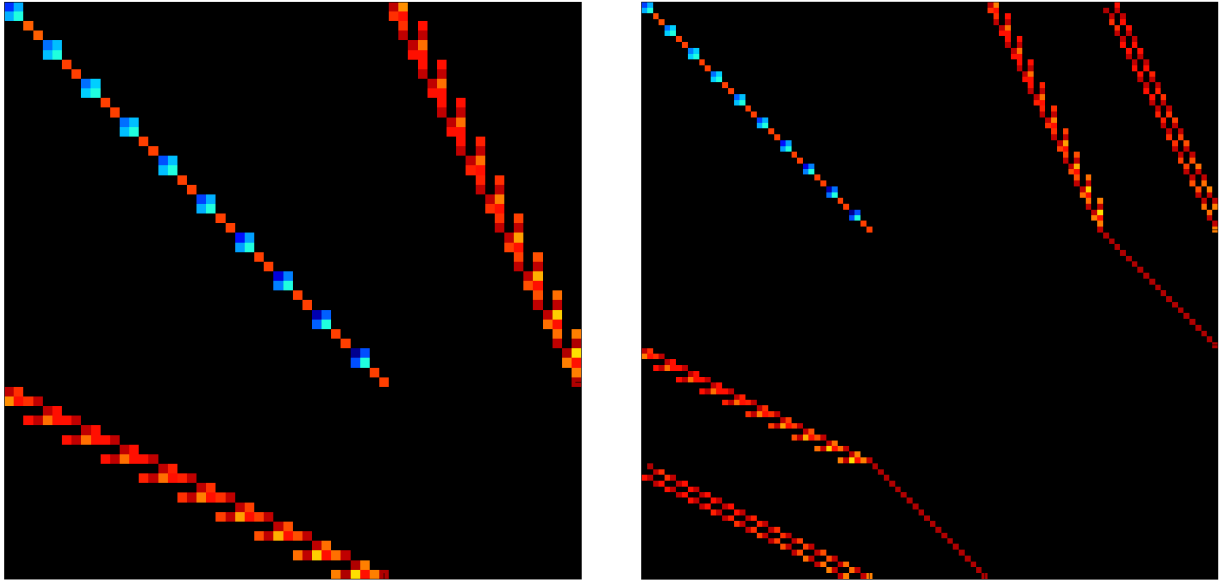
Figure 2: Block-banded structure of the system matrix in (1) (left) and in (6) (right).
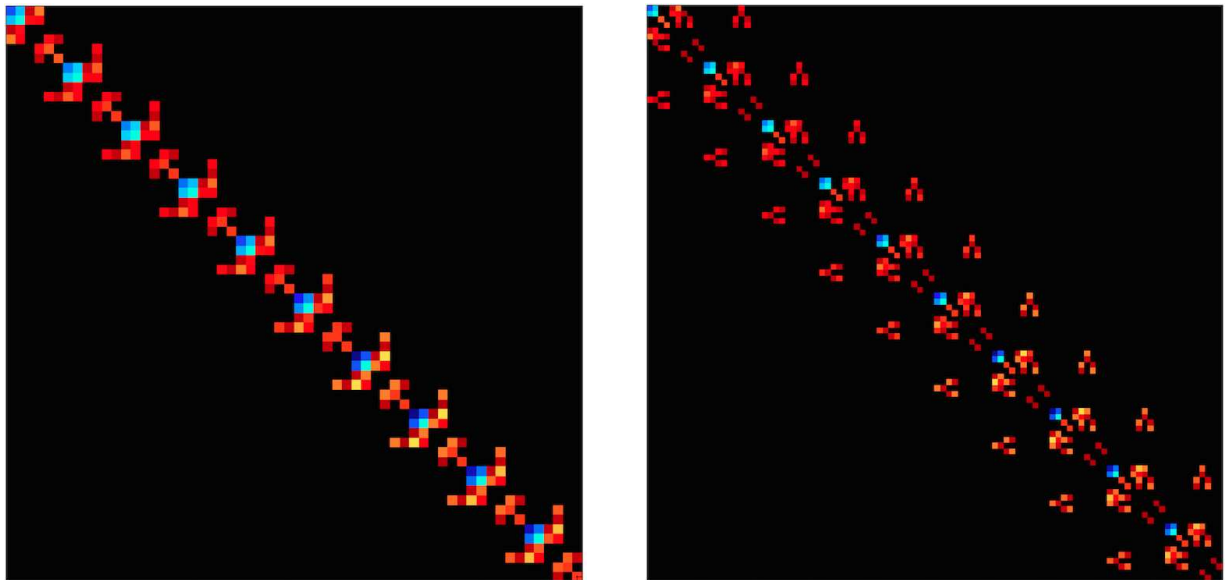
Figure 3: Banded structure of the system matrix in (1) (left) and in (6) (right) after reordering.

with the Jacobian $\boldsymbol{\Phi}(\boldsymbol{q}) = \nabla\boldsymbol{\varphi}(\boldsymbol{q})$ and the minimal mass matrix

$$\boldsymbol{\mathcal{M}}(\boldsymbol{q}) = \boldsymbol{\Phi}(\boldsymbol{q})^\top \boldsymbol{M}(\boldsymbol{p})\boldsymbol{\Phi}(\boldsymbol{q})\big|_{\boldsymbol{p}=\boldsymbol{\varphi}(\boldsymbol{q})}. \tag{5}$$

Note that the columns of $\boldsymbol{\Phi}(\boldsymbol{q})$ span the null space of $\boldsymbol{G}(\boldsymbol{\varphi}(\boldsymbol{q}))$. Especially, we have $\boldsymbol{G}(\boldsymbol{\varphi}(\boldsymbol{q}))\boldsymbol{\Phi}(\boldsymbol{q}) \equiv \boldsymbol{0}$. By the use of BDF-multistep methods, system (4) needs not necessarily be solved for $\ddot{\boldsymbol{q}}$, which would yield a complexity of order $\mathcal{O}(N^3)$ for the numerical linear algebra in each time step. However, the effort in linear algebra grows like $\mathcal{O}(N^2)$, since the mass matrix is fully populated [1, 3], see Figure 4 on the right.

Figure 4: Due to the use of joint coordinates the null space matrix $\boldsymbol{\Phi}(\boldsymbol{q})$ has triangular structure (left). The minimal mass matrix $\boldsymbol{\mathcal{M}}(\boldsymbol{q})$ in (5) is full (right).

Third approach   It is formulated in terms of so-called *mixed coordinates*, as it is introduced in [1] for applications in multibody dynamics. System

$$
\begin{bmatrix} \ddot{\boldsymbol{p}} \\ \ddot{\boldsymbol{q}} \\ \boldsymbol{\lambda} \\ \boldsymbol{\eta} \end{bmatrix} = \begin{bmatrix} \boldsymbol{M}(\boldsymbol{p}) & \boldsymbol{0} & \boldsymbol{G}(\boldsymbol{p})^\top & -\boldsymbol{\Psi}(\boldsymbol{p})^\top \\ \boldsymbol{0} & \boldsymbol{0} & \boldsymbol{0} & \boldsymbol{E} \\ \boldsymbol{G}(\boldsymbol{p}) & \boldsymbol{0} & \boldsymbol{0} & \boldsymbol{0} \\ -\boldsymbol{\Psi}(\boldsymbol{p}) & \boldsymbol{E} & \boldsymbol{0} & \boldsymbol{0} \end{bmatrix}^{-1} \begin{bmatrix} \boldsymbol{f}(\boldsy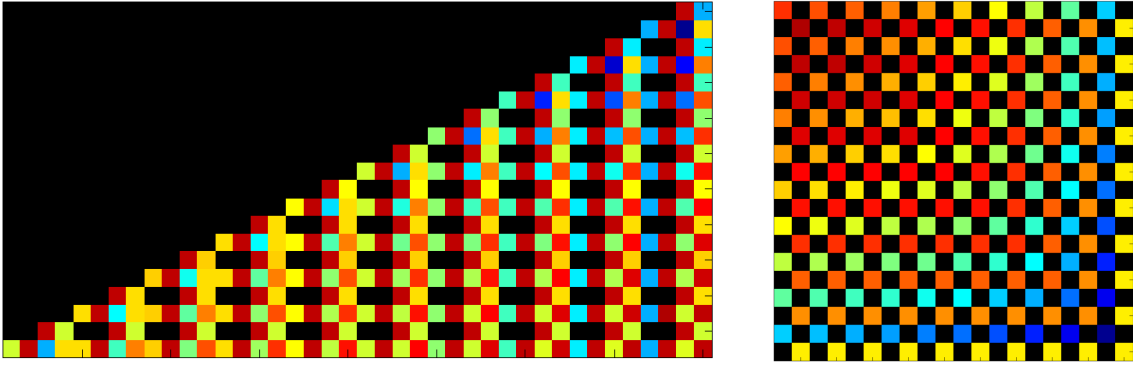mbol{p}, \dot{\boldsymbol{p}}, t) \\ \boldsymbol{0} \\ -\dot{\boldsymbol{G}}(\boldsymbol{p}, \dot{\boldsymbol{p}})\dot{\boldsymbol{p}} \\ \dot{\boldsymbol{\Psi}}(\boldsymbol{p}, \dot{\boldsymbol{p}})\dot{\boldsymbol{p}} \end{bmatrix}_{\boldsymbol{p}=\boldsymbol{\varphi}(\boldsymbol{q}), \dot{\boldsymbol{p}}=\boldsymbol{\Phi}(\boldsymbol{q})\dot{\boldsymbol{q}}} \tag{6}
$$

with the Jacobian $\boldsymbol{\Psi}(\boldsymbol{p}) = \nabla\boldsymbol{\psi}(\boldsymbol{p})$, is equivalent to (1). To see this, note that the analytic solution for the artificial Lagrange multiplier $\boldsymbol{\eta}$ is $\boldsymbol{\eta}(t) \equiv \boldsymbol{0}$. The effort for solving the linear system of equations in (6) in each time step grows with complexity $\mathcal{O}(N)$, since the structure is block-banded [3]. However, the bandwidth – after reordering – is 16 and thus larger than the one in (1), which is only 6, see Figure 3.
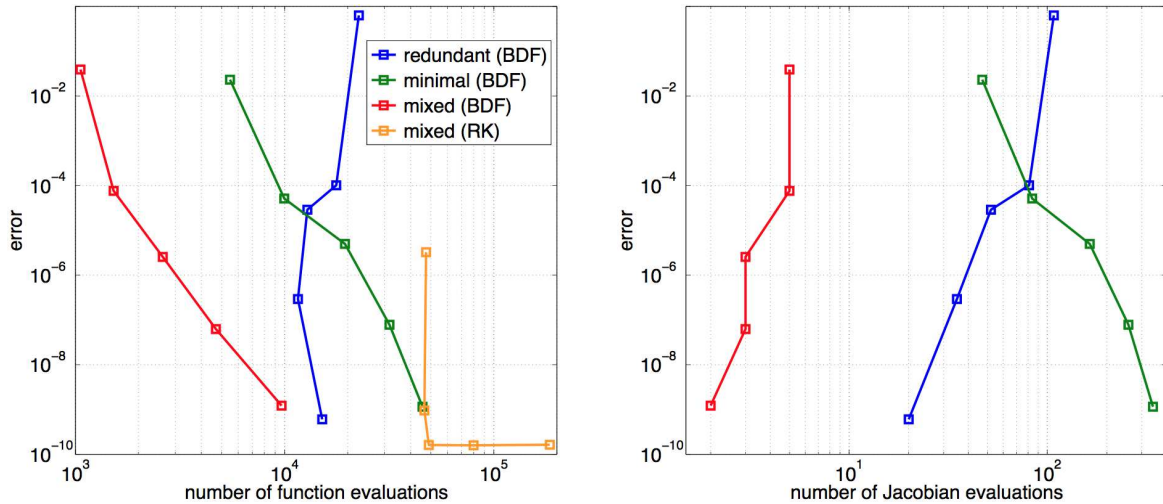
Figure 5: Numerical effort in terms of right-hand-side function evaluations (left) and Jacobian evaluations (right).

As can be seen from the numerical experiments in MATLAB displayed in Figure 5, the mixed coordinate formulation yields promising results – roughly a saving factor of 10 – concerning accuracy and numerical complexity, estimated from the number of right-hand-side function and Jacobian evaluations. Here, 'BDF' denotes the MATLAB time integrator ODE15s, a variable order multistep method based

on well-known backward differentiation formulas of order 1 to 5, see [4]. 'RK' denotes the MATLAB solver ODE45, based on the explicit embedded Runge-Kutta scheme of Dormand and Prince [4]. However, the computational amount of linear algebra needed to solve (1) and (6) in each time step has to be taken into account in order to quantify the total numerical task objectively. This is the topic of current research.

References

[1] E. Eich-Soellner, and C. Führer. *Numerical methods in multibody dynamics.* Teubner, 1998.

[2] H. Lang, and M. Arnold. *Numerical aspects in the dynamic simulation of geometrically exact rods.* Applied numerical mathematics, Vol. 62(3), pp. 1411-1427, 2012.

[3] G. Golub, and C. Van Loan. *Matrix computations.* Third edition, John Hopkins university press, 1996.

[4] L.F. Shampine, and M.W. Reichelt. *The Matlab ODE suite.* SIAM journal on scientific computing, Vol. 18(1), pp. 1-22, 1997.

Exponential variational integrators for split potential systems

Odysseas Kosmas, Sigrid Leyendecker

In many Hamiltonian systems, the potential energy function is composed of different parts with strongly varying dynamics. As an example, in classical molecular dynamics, the potential energy includes contributions of several types of atomic interaction. These interactions lead to extremely stiff potentials which force the solution of the equations of motion to oscillate on a very small time scale [1].
Following [1, 2], in order to derive numerical integration schemes for these systems, we split their potential energy into a fast and a slow component. For the resulting Hamilton function, we derive a family of higher order exponential variational integrators that use different quadrature rules in the discrete action corresponding to the different potentials.

Review of variational integrators using interpolation techniques

For the derivation of high order variational integrators, we recall the discrete variational calculus [3]. A discrete Lagrangian is a map $L_d : Q \times Q \to \mathbb{R}$ which may be considered as an approximation of a continuous action with Lagrangian $L : TQ \to \mathbb{R}$, i.e. $L_d(q_k, q_{k+1}) \approx \int_{t_k}^{t_{k+1}} L(q, \dot{q})dt$. The action sum $S_d : Q^{N+1} \to \mathbb{R}, N \in \mathbb{N}$ corresponding to the Lagrangian L_d is defined as $S_d(\gamma_d) = \sum_{k=0}^{N-1} L_d(q_k, q_{k+1})$, with $\gamma_d = (q_0, \ldots, q_N)$ representing the discrete trajectory. The discrete Hamilton principle states that a motion γ_d of the discrete mechanical system extremizes the action sum, i.e. $\delta S_d = 0$. By differentiation and rearrangement of the terms and having in mind that both q_0 and q_N are fixed, the discrete Euler-Lagrange equations (DEL) are obtained [3]

$$D_2 L_d(q_{k-1}, q_k) + D_1 L_d(q_k, q_{k+1}) = 0, \qquad k = 1, \ldots, N-1 \tag{1}$$

where the notation $D_i L_d$ indicates the slot derivative with respect to the i-th argument of L_d. The definition of the discrete conjugate momentum at time steps k and $k+1$ reads $p_k = -D_1 L_d(q_k, q_{k+1})$, $p_{k+1} = D_2 L_d(q_k, q_{k+1}), k = 0, \ldots, N-1$. The latter equations, also known as

position-momentum form of a variational integrator, can be used when an initial condition (q_0, p_0) is known, to obtain (q_1, p_1).

To construct high order methods, we approximate the action integral along the curve segment between q_k and q_{k+1} using a discrete Lagrangian that depends only on the end points. We obtain expressions for configurations q_k^j and velocities $\dot{q}_k^j$ for $j = 0, \ldots, S-1$, $S \in \mathbb{N}$ at time $t_k^j \in [t_k, t_{k+1}]$ by expressing $t_k^j = t_k + C_k^j h$ for $C_k^j \in [0, 1]$ such that $C_k^0 = 0, C_k^{S-1} = 1$ using

$$q_k^j = g_1(t_k^j) q_k + g_2(t_k^j) q_{k+1}, \qquad \dot{q}_k^j = \dot{g}_1(t_k^j) q_k + \dot{g}_2(t_k^j) q_{k+1}, \tag{2}$$

where $h \in \mathbb{R}$ is the time step. We choose functions

$$g_1(t_k^j) = \sin\left(u - \frac{t_k^j - t_k}{h} u\right) (\sin u)^{-1}, \quad g_2(t_k^j) = \sin\left(\frac{t_k^j - t_k}{h} u\right) (\sin u)^{-1}, \tag{3}$$

to represent the oscillatory behavior of the solution, see [4]. For continuity, $g_1(t_{k+1}) = g_2(t_k) = 0$ and $g_1(t_k) = g_2(t_{k+1}) = 1$ is required.

For any choice of interpolation used, we define the discrete Lagrangian by the weighted sum $L_d(q_k, q_{k+1}) = h \sum_{j=0}^{S-1} w^j L(q_k^j, \dot{q}_k^j)$, where it can be easily proved that for maximal algebraic order $\sum_{j=0}^{S-1} w^j (C_k^j)^m = \frac{1}{m+1}$, where $m = 0, 1, \ldots, S-1$ and $k = 0, 1, \ldots, N-1$ see [4].

Applying the above interpolation technique with the trigonometric expressions (3), following the phase lag analysis of [4], the parameter u can be chosen as $u = \omega h$. For problems that include a constant and known domain frequency ω (such as the harmonic oscillator) the parameter u can be easily computed. For the solution of orbital problems of the general N-body problem, where no unique frequency is given, a new parameter u must be defined by estimating the frequency of the motion of every moving point mass [4].

Exponential integrators

We now consider the Hamiltonian systems

$$\ddot{q} + \Omega q = g(q), \qquad g(q) = -\nabla U(q), \tag{4}$$

where Ω is a diagonal matrix and $U(q)$ is a smooth potential function. We are interested in the long time behavior of numerical solutions when ωh is not small.

Since $q_{k+1} - 2\cos(h\omega) q_k + q_{k-1} = 0$ is an exact discretisation of (4), see [5], we can consider the numerical scheme

$$q_{k+1} - 2\cos(h\omega) q_k + q_{k-1} = h^2 \psi(\omega h) g(\phi(\omega h) q_k), \tag{5}$$

where the functions $\psi(\omega h)$ and $\phi(\omega h)$ are even, real-valued functions satisfying $\psi(0) = \phi(0) = 1$, see [1]. The resulting methods using the latter numerical scheme are known as exponential integrators (for some examples of those integrators see [1]).

Exponential high order variational integrators   If we now use the phase fitted variational integrator in (4), the discrete Euler-Lagrange equations (1) read

$$q_{k+1} + \Lambda(u, \omega, h, S) q_k + q_{k-1} = h^2 \Psi(\omega h) g(\Phi(\omega h) q_k), \tag{6}$$

where

$$\Lambda(u, \omega, h, S) = \frac{\sum_{j=0}^{S-1} w^j \left[\dot{g}_1(t_k^j)^2 + \dot{g}_2(t_k^j)^2 - \omega^2 \left(g_1(t_k^j)^2 + g_2(t_k^j)^2 \right) \right]}{\sum_{j=0}^{S-1} w^j \left[\dot{g}_1(t_k^j) \dot{g}_2(t_k^j) - \omega^2 g_1(t_k^j) g_2(t_k^j) \right]}. \tag{7}$$
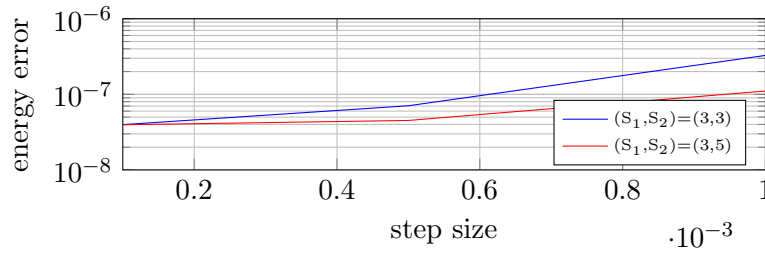
Figure 1: Modified satellite solar system. Global error for the energy error using the proposed family of exponential methods (red line) for $S_1 = 3$, $S_2 = 5$ and the ones that use $S = 3$ (blue line).

Exponentially fitted methods using phase fitted variational integrators can be derived when

$$\Lambda(u, \omega, h, S) = -2\cos(\omega h). \tag{8}$$

holds. Thus, phase fitted variational integrators using trigonometric interpolation can be considered as exponential integrators.

Family of higher order exponential variational integrators for split potential systems

We focus in the derivation of a family of exponential high order variational integrators for systems containing slow and fast potentials. Following [1, 2], we split the potential energy of the Lagrangian to fast and slow terms, i.e.

$$L(q, \dot{q}) = T(\dot{q}) - V^f(q) - V^s(q), \tag{9}$$

where $T(\dot{q}) = \frac{1}{2}\dot{q}^T M \dot{q}$ is the kinetic energy of the system (M is a constant mass matrix). In order to use different quadrature rules to approximate the contribution of each potential to the action, we use different numbers of intermediate points for each potential. Denoting the numbers of intermediate points for the slow and the fast potential by S_1 and S_2 respectively, we restrict ourselves to choices that $S_1 < S_2$ (the choice $S_1 = S_2$ creates the exponential integrators of [?, 4]).
Following [4] the discrete Lagrangian corresponding to (9) is

$$L_d^{S_1, S_2}(q_k, q_{k+1}) = h\left[\sum_{j=0}^{S_1-1} w_1^j\left[T(\dot{q}(t_k^j)) - V^s(q(t_k^j))\right] - \sum_{j=0}^{S_2-1} w_2^j V^f(q(t_k^j))\right], \tag{10}$$

where intermediate positions and velocities are given in (2) and (3), for $S = S_1$ and $S = S_2$ respectively.

Satellite solar system

As a numerical example, we choose the modified solar system with two planets (with masses $m_1 = 1$ and $m_2 = m_3 = 10^{-2}$) and a satellite ($m_4 = 10^{-4}$) which moves rapidly around the mass m_2, see [1]. Considering initial configurations $q_1 = (0, 0)$, $q_2 = (1, 0)$, $q_3 = (4, 0)$, $q_4 = (1.01, 0)$ and initial velocities $\dot{q}_1 = (0, 0)$, $\dot{q}_2 = (0, 1)$, $\dot{q}_3 = (0, 0.5)$, $\dot{q}_4 = (0, 0)$, the motion of the two planets is nearly circular with periods close to 2π and 14π, respectively [1]. The problem is then described by the Lagrange function

$$L(q, \dot{q}) = \frac{1}{2}\sum_{i=1}^{4} m_i \dot{q}_i^2 - V^f(q) - V^s(q), \tag{11}$$

where

$$V^s(q) = \sum_{i<j,(i,j)\neq(2,4)}^{4} \frac{m_i m_j}{||q_i - q_j||}, \qquad V^f(q) = \frac{m_2 m_4}{||q_2 - q_4||}. \tag{12}$$

Figure 1 shows the comparison of errors in total energy of the system at $t = 1$ for time steps $h \in \{10^{-4}, 5 \cdot 10^{-4}, 10^{-3}\}$ for the proposed family of exponential methods (red line) for $S_1 = 3$, $S_2 = 5$ and the ones that use $S = 3$ (blue line), see [4]. In that, it is clear that for all the step sizes that are tested, the smallest energy errors are obtained when using the splitting technique.

References

[1] E. Hairer, C. Lubich, and G. Wanner. *Geometric numerical integration illustrated by the Störmer-Verlet method.* Acta Numerica, Vol. 12, pp. 399-450, 2003.

[2] A. Stern, and E. Grinspun. *Implicit-explicit integration of highly oscillatory problems.* Multiscale Modeling and Simulation, Vol. 7, pp. 1779-1794, 2009.

[3] J. Marsden, and M. West. *Discrete mechanics and variational integrators.* Acta Numerica, Vol. 10, pp. 357-514, 2001.

[4] O.T. Kosmas, and S. Leyendecker. *Phase lag analysis of variational integrators using interpolation techniques.* PAMM Proc. Appl. Math. Mech., Vol. 12, pp. 677-678, 2012.

[5] R.P. Agarwal. *Difference equations and inequalities: Theory, Methods, and Applications.* Marcel Dekker, New York, 1992.

Characterizing rigidity in biomolecules with geometric tools

Dominik Budday, Sigrid Leyendecker, Henry van den Bedem

Proteins perform their function or interact with partners by changing between conformational substates on a wide range of spatiotemporal scales. Structurally characterizing these changes is challenging, both experimentally and computationally. While molecular dynamics (MD) simulations can provide atomically detailed insight into the dynamics, computational demands to adequately sample conformational ensembles of large biomolecules and their complexes often require tremendous resources. By contrast, kinematic models are computationally inexpensive and can provide high-level insights into conformational ensembles and molecular rigidity beyond the reach of MD simulations.

We model a protein as a kinematic linkage, with groups of atoms as rigid bodies and covalent, rotatable bonds as links with a torsional degree of freedom (DoF) [1, 2]. Hydrogen bonds are encoded as additional constraints only allowing a rotation about their bond axis, which lead to nested, interdependent cycles that require coordinated changes of the torsional angles. The configuration vector $\boldsymbol{q} \in \mathbb{R}^n$ consists of all n torsional angles in the molecule and describes the current configuration. Cycle-closing hydrogen bonds are modelled as holonomic constraints $\boldsymbol{\Phi}(\boldsymbol{q}) = \boldsymbol{0} \in \mathbb{R}^{5m}$, leading to a description of the constraint manifold in the form of $Q = \{\boldsymbol{q} \in \mathbb{R}^n \mid \boldsymbol{\Phi}(\boldsymbol{q}) = \boldsymbol{0}\}$ with five constraint equations for each of the m cycles. The holonomic constraints entail kinematic or hidden constraints as they have to comply with the consistency condition $\mathrm{d}\boldsymbol{\Phi}/\mathrm{d}t = \boldsymbol{0}$. These take the form

$$\mathbf{J}\dot{\boldsymbol{q}} = \boldsymbol{0}, \tag{1}$$

with the constraint Jacobian matrix $\mathbf{J}$ and angular velocities $\dot{\boldsymbol{q}}$. All admissible instantaneous velocities lie in the tangent space $T_q Q$ [3] that forms a subspace of dimension $n - r$, where r is the rank of the

Jacobian matrix, i.e. the number of independent constraint equations. In view of (1), it is identical to the nullspace of the constraint Jacobian,

$$T_q Q = null\left(\mathbf{J}(\boldsymbol{q})\right). \tag{2}$$

Introducing the nullspace matrix $\mathbf{N}(\boldsymbol{q}) \in \mathbb{R}^{n \times (n-r)}$ as an orthonormal basis for the nullspace, we obtain a direct mapping from generalized velocities of the floppy modes $\boldsymbol{u} \in \mathbb{R}^{n-r}$ onto admissible velocities $\dot{\boldsymbol{q}}_{\mathrm{N}}$ of the configuration, such that

$$\dot{\boldsymbol{q}}_{\mathrm{N}} = \mathbf{N}\dot{\boldsymbol{u}}. \tag{3}$$

This leads to a direct separation of rigidified and coordinately rotating torsional angles:

1. Locked torsional angles have zero velocity. Hence, the corresponding row in $\mathbf{N}$ only contains entries equal to zero.

2. Coordinated torsional angles experience rotation and encounter non-zero entries in their corresponding row.

We compute a basis for the nullspace using a singular value decomposition (SVD). The SVD uniquely decomposes the Jacobian matrix as $\mathbf{J} = \mathbf{U}\mathbf{\Sigma}\mathbf{V}^T$, with a $5m \times n$ diagonal matrix $\mathbf{\Sigma}$ containing the singular values and quadratic matrices $\mathbf{U}$ and $\mathbf{V}$ comprising the left- and right-singular vectors, respectively. The columns $r+1$ to n of $\mathbf{V}$ form an orthonormal basis of the nullspace.
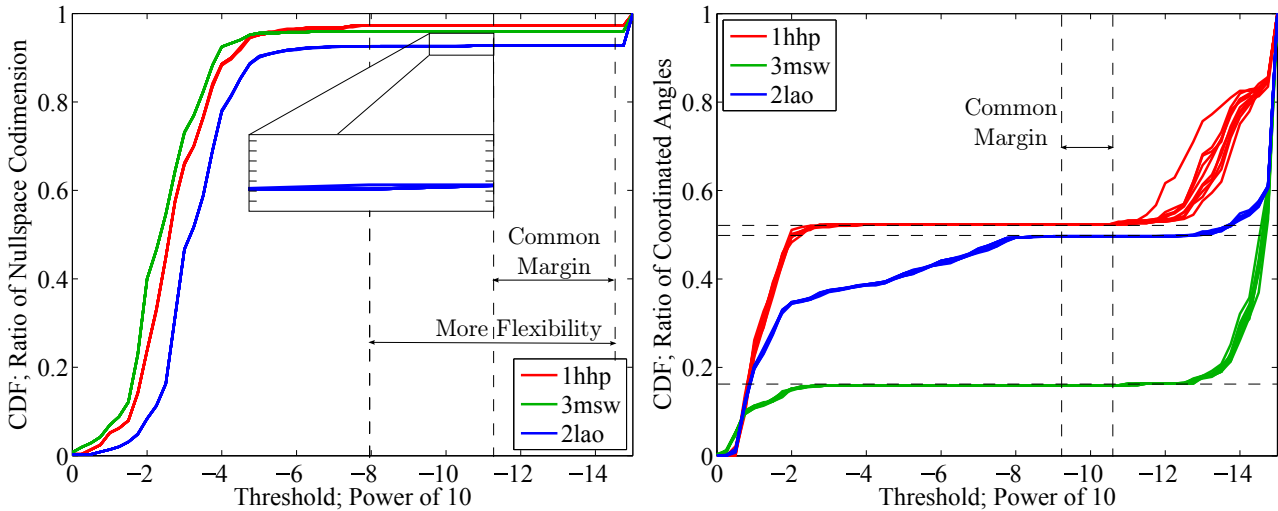
Figure 1: The left panel shows the CDF of normalized singular values for three different test proteins and ten samples each. A common margin of several orders of magnitude allows a clear separation of the vanishing singular values. LAO binding protein (2lao) features a very small singular value, shown in the enlarged area, indicating proximity to a singular configuration. The right panel shows the CDF for the largest entry in magnitude of each row of the nullspace matrix. Torsional angles whose corresponding row has a maximum value above the threshold are considered moveable. We find a common margin where the number of rigidified and coordinated angles is constant for all test proteins, allowing to separate the rigidified DoFs.

We investigate the probability distribution of the singular values to determine suitable thresholds for the nullspace computation. The left panel of Figure 1 shows the empirical cumulative distribution

function (CDF) for the normalized singular values, obtained from the SVD of the Jacobian matrices of three test proteins (PDB codes $3msw$, $1hhp$ and $2lao$) with ten different samples each. The distributions feature a common margin where the pro rata nullspace dimension is constant. Choosing a threshold value τ within this gap clearly separates zero-valent from non-zero singular values and correctly identifies the physical nullspace. LAO binding protein ($2lao$), the biggest of the three test proteins, mostly limits the margin, due to a very small singular value shown in the enlarged area. This suggests that the protein configuration is close to a singularity. Choosing a threshold above this value shows how singularities affect molecular rigidity and can lead to a different set of rigid clusters. Subsequent to the identification of the nullspace dimension and matrix, we require a distinct separation of rigidified and moveable DoFs. The right panel of Figure 1 shows the empirical CDF for the largest entry in magnitude of each row of the nullspace matrix. Rows with maximum values above the threshold belong to coordinately moving angles. Results are obtained from the same data set and based upon a threshold value $\tau = 1e - 12$, lying within the previously identified margin. We find a similar, yet smaller common margin, admitting a unique identification of the rigidified and coordinately moving DoFs. We introduce a second parameter μ as a threshold within the margin and use it simultaneously for the identification of locked hydrogen bonds. Overall, we obtain a robust numerical procedure for a complete rigidity analysis solely based on the nullspace matrix and two parameters.
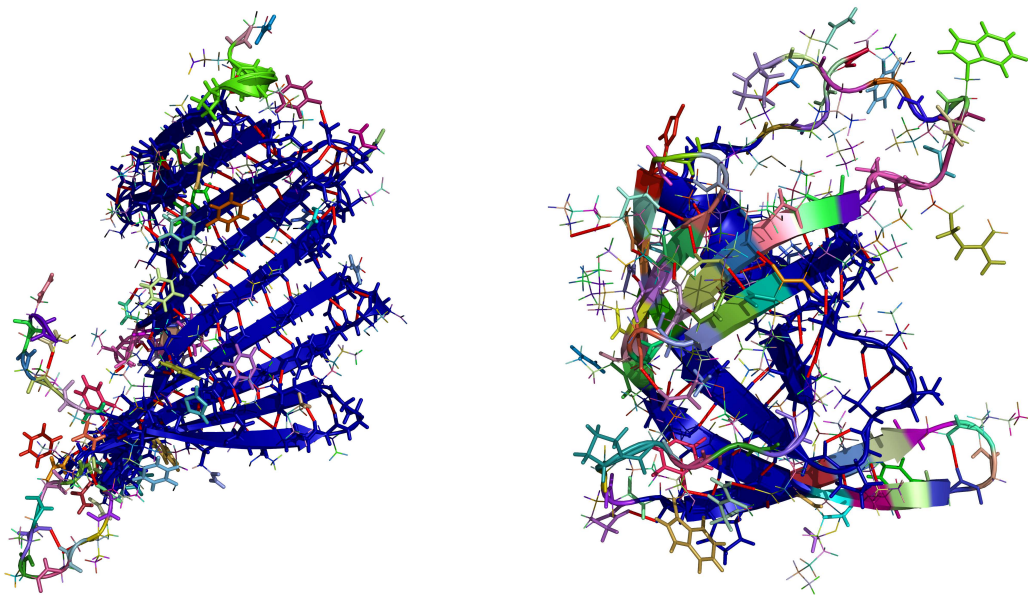
Figure 2: Rigid cluster decomposition with individual coloring. The biggest cluster is dark blue, hydrogen bonds are marked as red lines. Depicted are proteins with PDB codes $3msw$ (left) and $1hhp$ (right).

With the described procedure, we identify all rigidified torsional angles and the resulting set of rigid clusters. For validation, we compare our results with the KINARI webserver [4] and identify hydrogen bonds using their internal software with an energy threshold of -1.0kcal/mol. Other non-covalent bonding forces are not considered. We choose threshold parameters in agreement with the previous numerical analysis and find the exact same rigid cluster decomposition on an atomic level as KINARI. A basic overview on statistical measures of the three example proteins is given in Table 1, where d and n are the dimensions of the overall and constrained set of torsional angles, respectively, and $n-r$ is the number of remaining internal DoFs (floppy modes). We find the biggest rigid cluster with a total of 900 atoms in $3msw$, distributing the remaining floppy modes over only few participarting rotational angles.

The left panel in Figure 2 shows the $3msw$ rigid cluster decomposition with each color representing an individual rigid body. The large, dark blue β-meander motif is completely rigidified and forms the biggest cluster. We find a similar rigidification for the smaller β-meander motif in $1hhp$ that rigidly connects with the α-helix in the background (see Figure 2 right). The rainbow appearance of the three β-hairpins indicates multiple small clusters and thus, remaining flexibility.

Table 1: Basic statistics on rigidity analysis

PDB ID	# atoms	# h-bonds	# rigid clusters	| biggest cluster (atoms)|	n	n_{rigid}	$n-r$
1hhp	1563	58	412	335	321	144	39
3msw	2203	109	403	900	520	437	21
2lao	3608	188	929	215	934	470	68
2lao[*]	3608	188	982	215	934	416	69

[*] more flexible cutoff
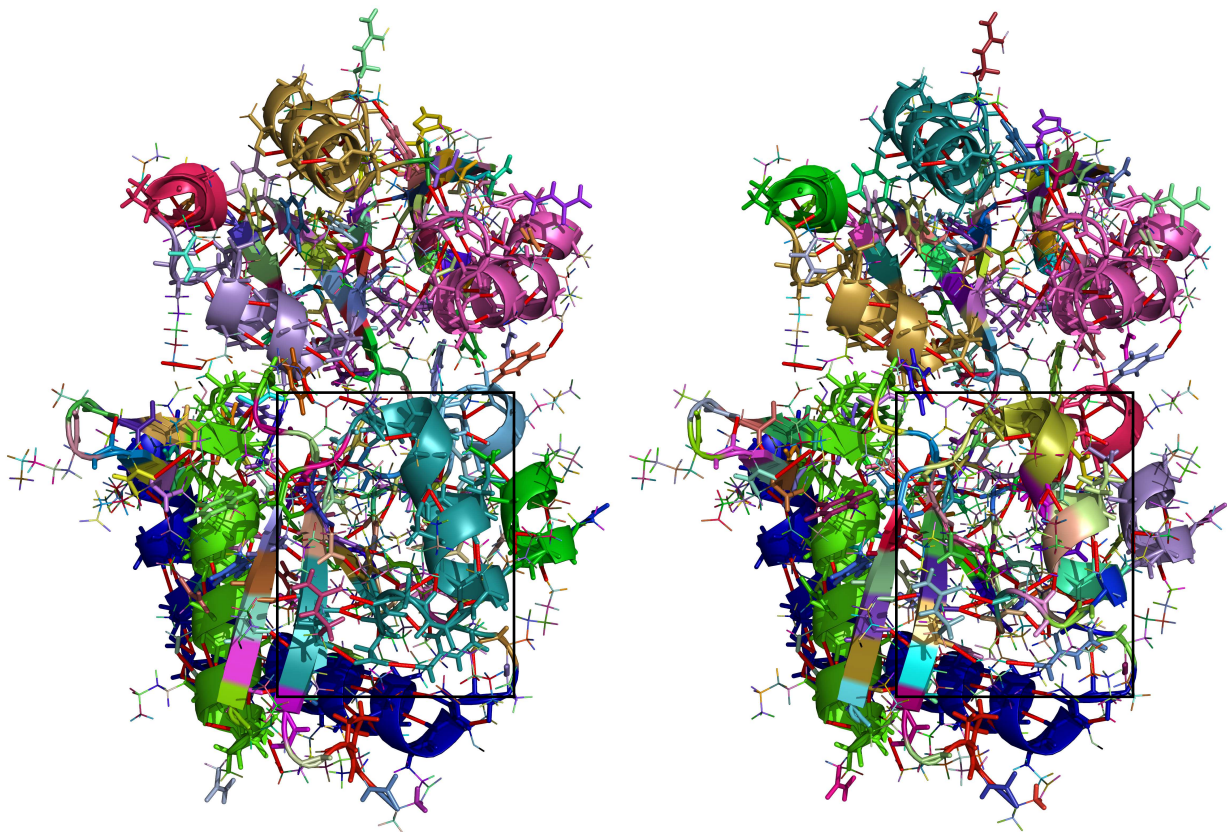
Figure 3: Rigid cluster decomposition of $2lao$ with individual coloring and hydrogen bond constraints as red lines. The left panel shows the generic result, obtained with parameters inside the common margin or KINARI. The large turquois cluster in the highlighted rectangle rigidly connects the α-helix to part of the adjacent β-strand. The right panel shows rigid clusters obtained with slightly relaxed threshold parameters. We identify the highlighted area where a previously large rigid cluster is now composed of multiple small clusters. All other clusters remain the same.

Figure 3 shows the set of rigid clusters in $2lao$, with the generic rigidity result that is equally obtained with our method and KINARI on the left side and less restricting cut-offs including the close-to-

singular motion on the right. We identify the change as a decomposition of the α-helix in the marked rectangle, i.e. the additional floppy mode is a coordinated flex of the helix. Parameter selection appears as an additional feature that identifies the effect of close-to-singular configurations on the rigidity of the molecule. All other rigid clusters are identical, although the color pattern changes with the new "by size" order of the clusters.

Explicit constraint counting as done in KINARI treats rigidity as a combinatorial problem, independent of the underlying geometry. This results in a very fast algorithm, but yields correct results only for generic configurations. The LAO binding protein example shows that singularities can lead to additional flexibility in the structure. Our geometric approach identifies rigidity from the tangent space of the constraint manifold and detects these effects. The nullspace also provides an explicit basis for coordinated motions along floppy modes, resulting in an efficient procedure to probe conformational space. Understanding how different parts of biomolecules are conformationally coupled will provide important knowledge to engineer or allosterically modulate biomolecules by selectively stabilizing conformations that enhance or inhibit function with broad implications for human health.

References

[1] P. Yao, L. Zhang, J.-C. Latombe. *Sampling-based exploration of folded state of a protein under kinematic and geometric constraints.* Proteins: Structure, Function, and Bioinformatics, Wiley Online Library, Vol. 80, pp. 25-43, 2012.

[2] R. Fonseca, D.V. Pachov, J. Bernauer, H. van den Bedem. *Characterizing RNA ensembles from NMR data with kinematic models.* Nucleic acids research, Oxford Univ Press, Vol. 42 (15), pp. 9562-9572, 2014.

[3] P. Betsch, S. Leyendecker. *The discrete null space method for the energy consistent integration of constrained mechanical systems. Part II: Multibody dynamics.* International journal for numerical methods in engineering, Wiley Online Library, Vol. 67, pp. 499-552, 2006.

[4] N. Fox, F. Jagodzinski, Y. Li, I. Streinu. *KINARI-Web: A Server for Protein Rigidity Analysis.* Nucleic Acids Research, Vol. 39, W177-W183, 2011.

On the role of quadrature rules and system dimensions in variational multirate integrators

Tobias Gail, Sina Ober-Blöbaum, Sigrid Leyendecker

For mechanical systems with dynamics on varying time scales, the numerical integration has to comply with contradicting requirements. On the one hand, to guarantee a stable integration of the fast motion, we need tiny step sizes. On the other hand, for the slow motions, a larger time step size is accurate enough. Furthermore, too small time steps increase the computing time unnecessarily, especially for costly function evaluations.

For this, multirate formulations split the system into subsystems [1] which can be solved with different methods [4]. To approximate the solution, rather than choosing one time grid we choose two time grids. Figure 3 shows such a time grid with macro time grid and and micro time grid. Here, the macro time step is ΔT, the micro time step is Δt and $\Delta T \geq \Delta t$ holds.

This is described in the framework of variational multirate integration [2] which is developed on the basis of variational integrators. This approach leads to a reduction of computing time, see [3]. However, the savings are not unlimited for arbitrary numbers of micro steps, meaning that there is a minimum

in computing time for a certain number of micro steps per macro step. In this work, it is investigated how this minimum is related to the number of degrees of freedom of a system i.e. to the systems's dimension. The limitations of the savings are investigated by means of the Fermi-Pasta-Ulam Problem (FPU) presented in Figure 2. Furthermore, numerical convergence is illustrated in Figure 5 for the triple spherical pendulum (TSP) in Figure 1.

Let a mechanical system be described by a Lagrangian with a configuration vector $q(t) \in Q \subseteq \mathbb{R}^n$ with Q a configuration manifold and a velocity vector $\dot{q} \in TQ \subseteq \mathbb{R}^n$ in the tangent space TQ. Also, let the mechanical system be constrained by the m^c-dimensional holonomic function of constraints requiring $g(q) = 0$. Now, let the mechanical system contain slow and fast dynamics, characterized by the possibility to split the variables into n^s slow variables q^s and n^f fast variables q^f with $q = (q^s, q^f)$ and $n = n^s + n^f$. Furthermore, we assume that we can split the potential energy into a slow potential $V(q)$ and a fast potential $W(q^f)$. The action S is the time integral of the Lagrangian $L(q, \dot{q}) = T(\dot{q}) - V(q) - W(q^f)$. Via Hamilton's principle requiring stationarity of the action $\delta S = 0$ the constrained multirate Euler-Lagrange equations are derived. Here, T denotes the kinetic energy and λ the Lagrange multiplier.

$$\frac{d}{dt}\frac{\partial T}{\partial \dot{q}^s} - \frac{\partial V}{\partial q^s} - \left(\frac{\partial g}{\partial q^s}\right)^T \cdot \lambda = 0$$

$$\frac{d}{dt}\frac{\partial T}{\partial \dot{q}^f} - \frac{\partial V}{\partial q^f} - \frac{\partial W}{\partial q^f} - \left(\frac{\partial g}{\partial q^f}\right)^T \cdot \lambda = 0$$

$$g(q) = 0 \qquad (1)$$
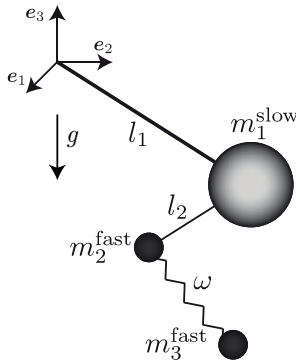
Figure 1: The triple spherical pendulum model with slow and fast variables.
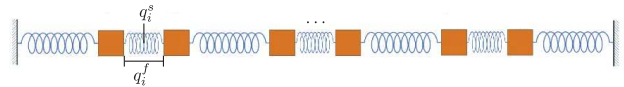
Figure 2: FPU with 6 masses and slow and fast variables.
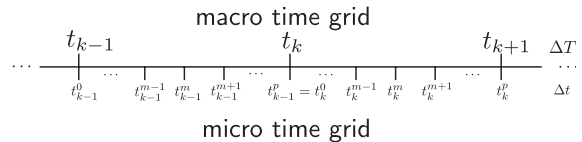
Figure 3: Macro and micro time grid.

The macro time grid provides the domain for the discrete slow variables $q_d^s = \{q_k^s\}_{k=0}^N$ with $q_k^s \approx q^s(t_k)$, while the micro time grid provides the domain for the discrete fast variables $q_d^f = \{\{q_k^{f,m}\}_{m=0}^p\}_{k=0}^{N-1}$ with $q_k^{f,m} \approx q^f(t_k^m)$. The domain for the discrete Lagrange multipliers is the macro and the micro grid, for example on the micro time grid $\lambda_d = \{\{\lambda_k^m\}_{m=0}^p\}_{k=0}^{N-1}$ with $\lambda_k^m \approx \lambda(t_k^m)$. The discrete Lagrangian and the discrete constraints approximate the action over one macro time step.

$$L_d(q_k^s, q_{k+1}^s, q_k^f, \lambda_k) \approx \int_{t_k}^{t_{k+1}} L(q, \dot{q})dt.$$

The sum over all time steps is the discrete action which approximates the continuous action. Via a discrete form of Hamilton's principle requiring stationarity for the discrete action, we derive the discrete constrained multirate Euler-Lagrange equations. These equations form a nonlinear set of equations which are solved using a Newton-Raphson method.
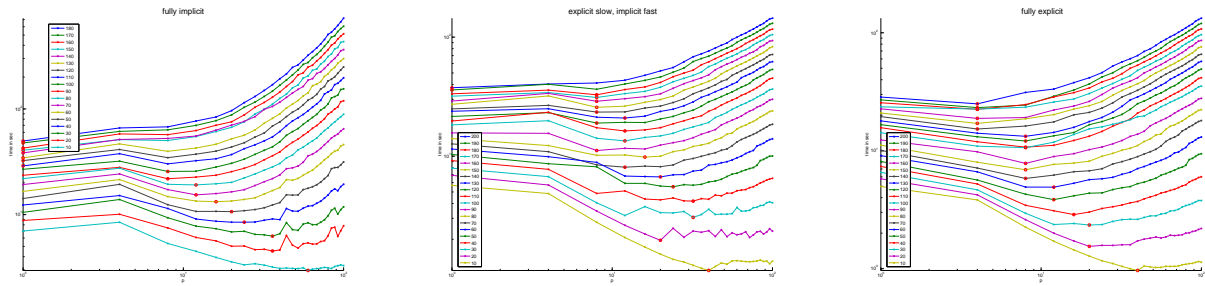
Figure 4: Computing time versus number of micro steps for the fully implicit (left) explicit slow, implicit fast (middle), and fully explicit scheme (right) with $p \in \{1, 4, 8, \ldots, 100\}$ and with $\ell \in \{10, 20, \ldots, 180\}$ for fully implicit and with $\ell \in \{10, 20, \ldots, 200\}$ for implicit slow, explicit fast and fully explicit.

Quadrature rules are needed to approximate the action and constraints by discrete quantities. We use e.g. the midpoint rule, the trapezoidal rule, an affine combination and finite difference. Different quadrature rules can be chosen for the kinetic energy, both potential energies and the constraints and lead to "fully implicit", "explicit slow, implicit fast" and "fully explicit" schemes.

We investigate the relation between the number of variables X and the number of micro steps per macro step p_{opt} at which the minimum of the computing time is achieved. For the investigation the FPU is used, see [3] for a model description and Figure 2. In order to get a varying number of variables $X$, the number of masses ℓ in the FPU is varied. For the FPU, half of the configuration variables are slow variables, the other half are fast variables, therefore $X = \frac{\ell}{2}(1 + p)$ holds. Figure 4 shows the computing time versus the number of micro steps with different lines for different numbers of ℓ, where ℓ increases from bottom to top curve. The minimum computing time is depicted with a red circle at every curve. In Figure 4, it is illustrated that for the fully implicit and the explicit slow, implicit fast scheme at $p_{opt} = 8$ and $p_{opt} = 12$, respectively and for the fully explicit scheme for $p_{opt} = 4$ and $p_{opt} = 8$, the minimum computing time is at the same p_{opt} for different ℓ. If the minimum computing time was depending on the number of variables, it would be at lower p for increasing ℓ. Because this is not the case, we conclude that the minimal computing time is not only depending on the number of variables X but is highly problem dependent. For a detailed comparison including different example systems see [3].
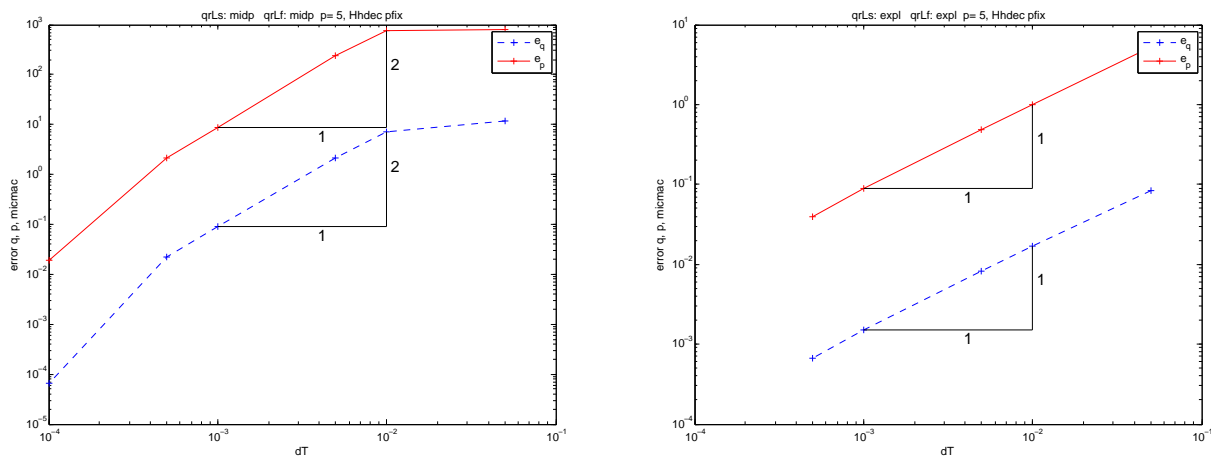

Figure 5: Error of configuration and conjugate momentum with $p = 5$ and $\Delta T \rightarrow 0$, $\Delta t \rightarrow 0$ for the fully implicit scheme (left) and the fully explicit scheme (right).

The convergence is shown numerically for the TSP for the fully implicit and the fully explicit quadrature schemes. Therefor, the global error

$$e_q = \sup_{\substack{k = 0, \ldots, N \\ m = 1, \ldots, p-1}} \{\|q_k - q(t_k)\|, \|q_k^{f,m} - q^f(t_k^m)\|\} \tag{2}$$

of the configuration as well as the error e_p of the conjugate momentum is plotted versus the time step. Figure 5 shows the convergence numerically for the TSP for the fully implicit and fully explicit scheme. For the fully implicit scheme Figure 5 shows on the left hand side convergence of order two. Convergence of order one is presented in Figure 5 on the right hand side for the fully explicit scheme.

References

[1] M. Arnold. *Multi-rate time integration for large scale multibodysystem models.* IUTAM Symposium on Multiscale Problems in Multibody System Contacts, P. Eberhard (ed), Vol. 195(50-51), pp. 1-10, Springer, 2007.

[2] S. Leyendecker, and S. Ober-Blöbaum. *A Variational approach to multirate integration for constrained systems.* Multibody Dynamics, Computational Methods in Applied Sciences, Computational Methods in Applied Sciences, J. C. Samin, P. Fisette (eds.), pp. 97-121, Springer, 2013.

[3] T. Gail, S. Leyendecker, and S. Ober-Blöbaum. *Computing time investigations of variational multirate integrators.* Proceedings of the Multibody Dynamics ECCOMAS Thematic conference, Zagreb, Croatia, pp. 603–612, 01–04 July 2013.

[4] A. Stern, and E. Grinspun. *Implicit-explicit variational integration of highly oscillatory problems.* Multiscale Model. Simul., Vol. 7(4), pp. 1779-1794, 2009.

Structure preserving optimal control of a 3d-dimensional upright gait

Michael W. Koch, Sigrid Leyendecker

The straight posture of the homo sapiens' gait is a characteristical attribute of the human species, whereby the evolution of the human gait results from an anthropological optimisation process. Initiated by climbing down from trees and leaving forests, the survival in velds necessitates a physical adoption and the results are reflected at the kind of human locomotion respectively at the physique: an upright gait shows benefits like a distinct all-round visibility and allows the possibility to use tools and weapons at the struggle of survival.

The goal of this work is to optimally control the human upright gait using a structure preserving variational integrator, whereby different physiologically motivated cost functions are tested. Based on Lagrangian mechanics, the action is discretised and with respect to the discrete variational principle the resulting discrete Euler-Lagrange equations are equipped with symplectic and momentum preserving properties. The discussed multibody system of an bipedal walker represents the consistent further development of the monopedal jumper models discussed in [1] and [2]. In the first citation, the simple footless monopedal jumper consists of three rigid bodies – upper part of the body, thigh and calf – consequently, a single point is used to model the contact. In [2], a more realistic behaviour is targeted, because the inclusion of the jumpers foot is a basic detail and it has enormous influence of the jumping movement before the contact between the foot and the ground is established or released. The properties of this monopedal jumper's leg are adopted to the multibody system of the bipedal walker.
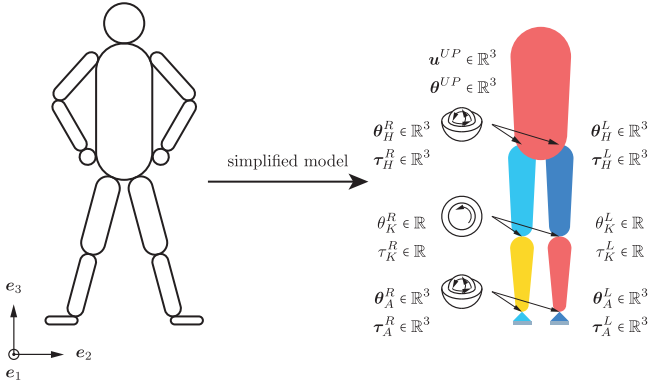
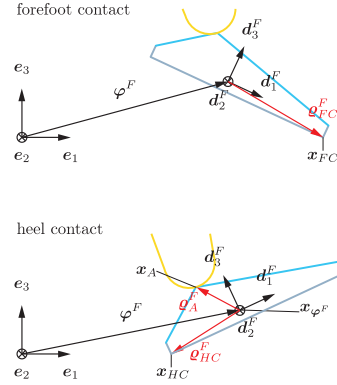Figure 1: Seven link model of the simplified bipedal walker.

Figure 2: Visualisation of the forefoot and heel contact of the walker's right leg.

Herein, the human upright gait is analysed using a simple model consisting of seven rigid bodies representing the human's torso plus the thigh, calf and foot of both legs, which are symmetrical to each other. The hips are modelled as spherical joints and the thigh and calf are chained with a revolute joint, where the unit vector $\boldsymbol{n}_1 \in \mathbb{R}^3$ specifies the axis of rotation of the knee. In reality, the human ankle joint has two rotational degrees of freedom, whose axis of rotation are diagonally located to each other – the implemented ankle joints are simplified using a spherical joint with anatomically adapted restrictions. The constrained multibody system is described by the configuration variable $\boldsymbol{q} \in \mathbb{R}^{84}$ and due to the rigid body formulation in use, $m_{int} = 42$ internal constraints are present. The joint interconnections cause $m_{ext} = 22$ external constraints and therefore the $k = 84$-dimensional system is restricted by $m = 64$ holonomic constraints. Corresponding to the $k - m = 20$ degrees of freedom, the generalised coordinates read $\boldsymbol{u} = \left[\boldsymbol{u}^{UP}; \boldsymbol{\theta}^{UP}; \boldsymbol{\theta}_H^R; \theta_K^R; \boldsymbol{\theta}_A^R; \boldsymbol{\theta}_H^L; \theta_K^L; \boldsymbol{\theta}_A^L\right]^T \in \mathbb{R}^{20}$ and $\boldsymbol{\tau} = \left[\boldsymbol{\tau}_H^R; \tau_K^R; \boldsymbol{\tau}_A^R; \boldsymbol{\tau}_H^L; \tau_K^L; \boldsymbol{\tau}_A^L\right]^T \in \mathbb{R}^{14}$ represents the actuation in the hip, knee and ankle joints of both legs (see Figure 1). The herein modelled feet have two contact points and thus three different contact scenarios are possible, i.e. two single contact phases (forefoot contact (FC), respectively, heel contact (HC)) as illustrated in Figure 2 and the complete contact support phase, at which the forefoot and the heel are in contact with the ground. Each contact point between the foot and the ground is fixed at the ground in $\mathbf{x}_i \in \mathbb{R}^3$ for $i = FC, HC$ by a spherical joint, consequently the contact function reads

$$\boldsymbol{g}_i^{(S)}\left(\boldsymbol{q}\right) = \boldsymbol{\varphi}^F + \boldsymbol{\varrho}_i^F - \boldsymbol{x}_i \in \mathbb{R}^3, \tag{1}$$

where $\boldsymbol{\varrho}_i^F$ points from the centre of mass to the respective contact point, while $\boldsymbol{\varrho}_A^F$ points to the ankle. The condition for double contact (FC and HC) is different from the contact formulation for one contact point in (1), because the combination of two spherical joints does not completely restrict the foot's degrees of freedom. The constructive approach used here is to fix one of the contact points at the ground by a spherical joint and for the other contact point, only the vertical component of the remaining spherical joint formulation is fixed. To prevent the residual rotational motions around the line connecting the FC and HC point, two further contact constraints are necessary, in this work the $\boldsymbol{e}_2$-component of the center of mass and of the ankle are picked; for example, the constraint formulation of the double contact phase (FHC) reads

$$\boldsymbol{g}_{FHC}\left(\boldsymbol{q}\right) = \begin{bmatrix} \boldsymbol{g}_{FC}^{(S)}\left(\boldsymbol{q}\right) \\ \left(\boldsymbol{e}_2\right)^T \cdot \left(\boldsymbol{\varphi}^F - \boldsymbol{x}_{\varphi^F}\right) \\ \left(\boldsymbol{e}_2\right)^T \cdot \left(\left(\boldsymbol{\varphi}^F + \boldsymbol{\varrho}_A^F\right) - \boldsymbol{x}_A\right) \\ \left(\boldsymbol{e}_3\right)^T \cdot \boldsymbol{g}_{HC}^{(S)}\left(\boldsymbol{q}\right) \end{bmatrix} = \boldsymbol{0} \in \mathbb{R}^6,$$

whereby the spherical joint formulation is exemplarily used at the forefoot and $\boldsymbol{x}_{\varphi F}, \boldsymbol{x}_A \in \mathbb{R}^3$ represent the location vectors where the center of mass and of the ankle are fixed in space.

The direct transcription method DMOCC is used to transform the optimal control problem into a constrained optimisation problem. The human gait can be considered as an examples of a hybrid system, where the dynamics is subject to an inherent switch due to the closing or opening of contacts at the feet. As specified in Figure 3, the motion sequence – not the switching time – in which the contact phases follow each other are considered as known. To perpetuate the structure preservation of the variational integrator and the geometrical correctness during the releasing and establishing of the contact at the feet, the non-smooth problem is solved including the computation of the contact or contact release configuration as well as the contact time and force, instead of relying on a smooth approximation of the contact problem via a penalty potential. Due to the cycle structure of human gait, only one half step is optimised, such that periodical boundary conditions are considered as equality conditions in the optimisation problem. The optimised course of motion with minimal control effort is shown in Figure 4.
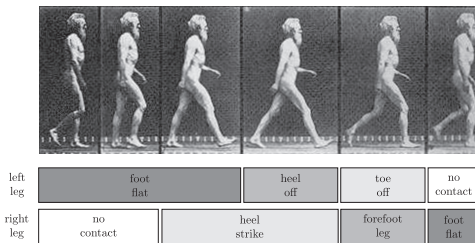
Figure 3: Characteristical configurations during the human bipedal walk.
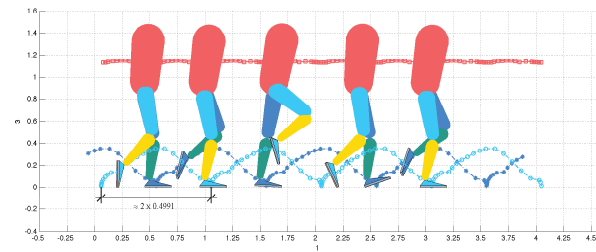
Figure 4: Snapshots of an optimised bipedal gait minimising the control effort.

References

[1] M. W. Koch, and S. Leyendecker. *Structure preserving simulation of monopedal jumping.* The archive of mechanical engineering, Vol. LX(1), pp. 127-146, 2013.

[2] M. W. Koch, and S. Leyendecker. *A structure preserving approach to the simulation of non-smooth dynamics.* PAMM, 2014, accepted.

Various quadrature rules for the approximation of the action integral in non-linear beam dynamics and elastostatics

Thomas Leitz, Sigrid Leyendecker

A beam is defined as a three dimensional object with a high length to cross-section area ratio. They are often used as structural elements, e.g. in bridges and buildings.

The configuration of a beam's cross-section is parameterized by the three dimensional position vector $x(s,t) \in \mathbb{R}^3$, representing the position of the gravitational center, and by a unit quaternion $p(s,t) \in \mathbb{H}^1 = \{p | p \in \mathbb{H}, \|p\| = 1\}$, representing the orientation. The arc length parameter is $s \in [0, \ell]$, where ℓ is the length of the beam, and the time parameter is $t \in [0, T]$, where $T > 0$ is some point in time. The translational velocity and strain are $\dot{x} = \frac{\mathrm{d}x}{\mathrm{d}t}$ and $x' = \frac{\mathrm{d}x}{\mathrm{d}s}$. The angular velocity is defined as $\omega = 2\bar{p} \circ \dot{p}$ and $\Omega = 2\bar{p} \circ p'$ is the angular strain. The angular velocity and strain are purely imaginary quaternions, i.e. $\omega, \Omega \in \mathfrak{h}^1 = \{f | f \in \mathbb{H}, \Re f = 0\}$. We define the deformation map $\varphi : (s,t) \to (p,x)$

which gives the position and the orientation of the cross-section at any point in space and time. The kinetic and potential energy densities for the beam are

$$T\left(p,\omega,x,\dot{x},s\right)=\frac{1}{2}\left(\rho\left(s\right)\|\dot{x}\|^{2}+\omega^{T}J\left(s\right)\omega\right)$$

$$V\left(p,\Omega,x,x',s\right)=\frac{1}{2}\left[\left(\bar{p}\circ x'\circ p-e_{3}\right)^{T}C_{1}\left(s\right)\left(\bar{p}\circ x'\circ p-e_{3}\right)+\Omega^{T}C_{2}\left(s\right)\Omega\right]+\rho\left(s\right)\langle x,[0,0,g]\rangle$$

where $\rho\left(s\right)$ is the line density, $J\left(s\right)$ is the mass moment of inertia density tensor, $C_{1}\left(s\right)=\operatorname{diag}\left(G\mathcal{A},G\mathcal{A},E\mathcal{A}\right)$, $G\left(s\right)$ is the shear modulus, $E\left(s\right)$ is the elongation modulus, $\mathcal{A}\left(s\right)$ is the cross-section area, $C_{2}=\operatorname{diag}\left(EI_{1},EI_{2},G\left(I_{1}+I_{2}\right)\right)$, $I_{1}\left(s\right),I_{2}\left(s\right)$ are the geometrical moments of inertia and g is the gravity constant.

Dynamics   The Lagrangian density for beam-dynamics reads

$$L\left(p,\omega,\Omega,x,\dot{x},x',s\right)=T\left(p,\omega,x,\dot{x},s\right)-V\left(p,\Omega,x,x',s\right)$$

The action is the integral of the Lagrangian density over space-time

$$S\left[\varphi\right]=\int_{0}^{T}\int_{0}^{\ell}L\mathrm{d}s\mathrm{d}t.$$

In order to derive a variational integrator [2], we discretize space-time using a regular grid as shown
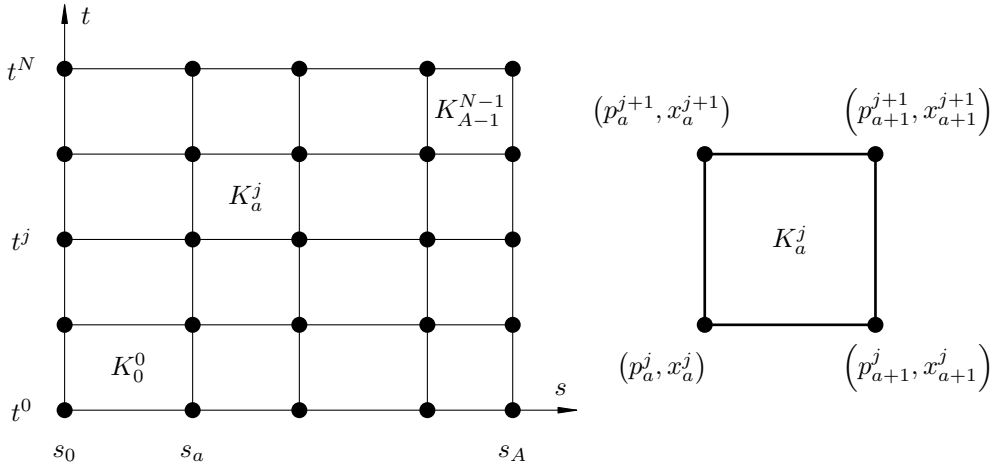
Figure 1: Discretization of space-time.

in Figure 1 with $\Delta s_{a}=s_{a+1}-s_{a}$ and $\Delta t^{j}=t^{j+1}-t^{j}$, where $a\in[0,A-1]\subset\mathbb{N}$ is the space index and $j\in[0,N-1]\subset\mathbb{N}$ is the time index. The positions are interpolated using element-wise bilinear functions $X_{a}^{j}\left(s,t\right)$ and the translational velocities and strains are $\dot{X}_{a}^{j}\left(s\right)$ and $X'^{j}_{a}\left(t\right)$ respectively. The quaternions are interpolated using element-wise bilinear functions divided by the length of the resulting four dimensional vector to ensure that $P_{a}^{j}\left(s,t\right)\in\mathbb{H}^{1}$. The angular velocities and strains are $\omega_{a}^{j}\left(s,t\right)=\bar{P}_{a}^{j}\left(s,t\right)\circ\dot{P}_{a}^{j}\left(s,t\right)$ and $\Omega_{a}^{j}\left(s,t\right)=\bar{P}_{a}^{j}\left(s,t\right)\circ P'^{j}_{a}\left(s,t\right)$. With $\mathcal{X}_{a}^{j}\left(s,t\right)=\left(P_{a}^{j},\omega_{a}^{j},\Omega_{a}^{j},X_{a}^{j},\dot{X}_{a}^{j},X'^{j}_{a}\right)$ the discrete Lagrangian is an approximation of the integral of the Lagrangian density over one space-time element using the weighted sum

$$L_{a}^{j}=\sum_{n=1}^{I}w_{n}L\left(\mathcal{X}_{a}^{j}\left(s_{a}^{n},t_{n}^{j}\right),s_{a}^{n}\right)\left(t^{j+1}-t^{j}\right)\left(s_{a+1}-s_{a}\right)\approx\int_{t^{j}}^{t^{j+1}}\int_{s_{a}}^{s_{a+1}}L\mathrm{d}s\mathrm{d}t. \tag{1}$$

Applying the discrete Hamilton's principle $\delta S_d = 0$ to the discrete action sum $S_d = \sum_{j=0}^{N-1} \sum_{a=0}^{A-1} L_a^j$ leads to the discrete Euler-Lagrange-equations [1]

$$\begin{bmatrix} \frac{1}{2}\Im\left(\bar{p}_a^j \circ \frac{\partial L_a^j}{\partial p_a^j} + \bar{p}_a^j \circ \frac{\partial L_a^{j-1}}{\partial p_a^j} + \bar{p}_a^j \circ \frac{\partial L_{a-1}^j}{\partial p_a^j} + \bar{p}_a^j \circ \frac{\partial L_{a-1}^{j-1}}{\partial p_a^j} \right) \\ \frac{\partial L_a^j}{\partial x_a^j} + \frac{\partial L_a^{j-1}}{\partial x_a^j} + \frac{\partial L_{a-1}^j}{\partial x_a^j} + \frac{\partial L_{a-1}^{j-1}}{\partial x_a^j} \end{bmatrix} = \begin{bmatrix} 0 \\ 0 \\ 0 \\ 0 \\ 0 \\ 0 \end{bmatrix}.$$

These can either be solved using the nodal reparametrization $p_a^{j+1} = p_a^j \circ \text{Cay}\left(f_a^j \right)$, where $\text{Cay}\left(f \right) = \frac{1+f}{\|1+f\|}$ is the quaternion Cayley map with its inverse $\text{Cay}^{-1}\left(p \right) = \frac{\Im p}{\Re p}$ with $f \in \mathfrak{h}^1$ and $p \in \mathbb{H}^1$ or by introducing algebraic constraints of the form $\frac{1}{2}\left[\left(p_a^{j+1} \right)^T p_a^{j+1} - 1 \right] = 0$ for $a = 0, \dots, A$.

Elastostatics The potential energy for the beam reads

$$\Pi\left(p, \Omega, x, x', s \right) = \int_0^\ell V \mathrm{d}s.$$

In order to derive a variational integrator, we discretize space using a regular grid with $\Delta s_a = s_{a+1} - s_a$, where $a \in [0, A-1] \subset \mathbb{N}$ is the space index. The positions are interpolated using element-wise linear functions $X_a(s)$ and the translational strains are X'_a. The quaternions are interpolated using element-wise linear functions divided by the length of the resulting four dimensional vector to ensure that $P_a(s) \in \mathbb{H}^1$. The angular strains are $\Omega_a(s) = \bar{P}_a(s) \circ P'_a(s)$. With $\mathcal{X}_a(s) = (P_a, \Omega_a, X_a, X'_a)$ the discrete potential energy of one element is an approximation of the integral of the potential energy density over one element using the weighted sum

$$V_a = \sum_{n=1}^I w_n V\left(\mathcal{X}_a\left(s_a^n \right), s_a^n \right)\left(s_{a+1} - s_a \right) \approx \int_{s_a}^{s_{a+1}} V \mathrm{d}s. \tag{2}$$

Applying the discrete Hamilton's principle $\delta \Pi_d = 0$ to the discrete potential energy $\Pi_d = \sum_{a=0}^{A-1} V_a$ leads to the static discrete Euler-Lagrange-equations

$$\begin{bmatrix} \frac{1}{2}\Im\left(\bar{p}_a \circ \frac{\partial V_a}{\partial p_a} + \bar{p}_a \circ \frac{\partial V_{a-1}}{\partial p_a} \right) \\ \frac{\partial V_a}{\partial x_a} + \frac{\partial V_{a-1}}{\partial x_a} \end{bmatrix} = \begin{bmatrix} 0 \\ 0 \\ 0 \\ 0 \\ 0 \\ 0 \end{bmatrix}.$$

These can be solved in the same way as the Euler-Lagrange equations for beam dynamics.

Results With the reparametrization of the space and time parameters s and t

$$t = (1-\alpha)t^j + \alpha t^{j+1} \qquad\qquad s = (1-\beta)s_a + \beta s_{a+1}, \tag{3}$$

where $\alpha, \beta \in [0, 1]$, we can define various quadrature rules for the discrete Lagrangian as listed in Table 1. These can be used for both the dynamic as well as the elastostatic integrators, though for elastostatics MPS will give the same result as MP and MPT will give the same result as GT.

Name	I	w	α	β
generalized trapezoidal (GT)	4	$\{0.25, 0.25, 0.25, 0.25\}$	$\{0, 0, 1, 1\}$	$\{0, 1, 0, 1\}$
midpoint (MP)	1	1	0.5	0.5
trapezoidal in time, midpoint in space (MPS)	2	$\{0.5, 0.5\}$	$\{0, 1\}$	$\{0.5, 0.5\}$
midpoint in time, trapezoidal in space (MPT)	2	$\{0.5, 0.5\}$	$\{0.5, 0.5\}$	$\{0, 1\}$

Table 1: Quadrature rules for the discrete Lagrangian (1) and potential energy (2) with (3)

As an example we consider a beam with on fixed end as shown in Figure 4. It is bearing its own weight denoted by $q = \rho bhg$ where ρ is the line density, b and h are the width and height of the beam and g is the gravity constant. The analytical solution of the differential equation of the bending line $EI_2 w'''' = q$ for this problem is

$$w\left(s\right) = \frac{\rho g}{EI_z}\left(\frac{1}{24}s^4 - \frac{1}{6}\ell s^3 + \frac{1}{4}\ell^2 s^2\right). \tag{4}$$

In Figure 2, we compare of the elastostatic integrator to $w\left(s\right)$. Even though GT and MPT converge to the real solution with an increasing number of nodes, they show significant shear locking, while MP and MPS do not show any locking and even the integration using only two nodes gives a good approximation for $w\left(\ell\right)$. This locking effect also appears in the dynamic simulation. To show this, we use the beam as shown in Figure 4 with a straight beam and zero velocities as initial conditions. Due to gravity, the beam exhibits a swinging motion and since GT and MPT again lead to shear locking, the frequency of the swinging motion is higher than using MP or MPS. The different frequencies can be observed in the energy plots shown in Figure 3.
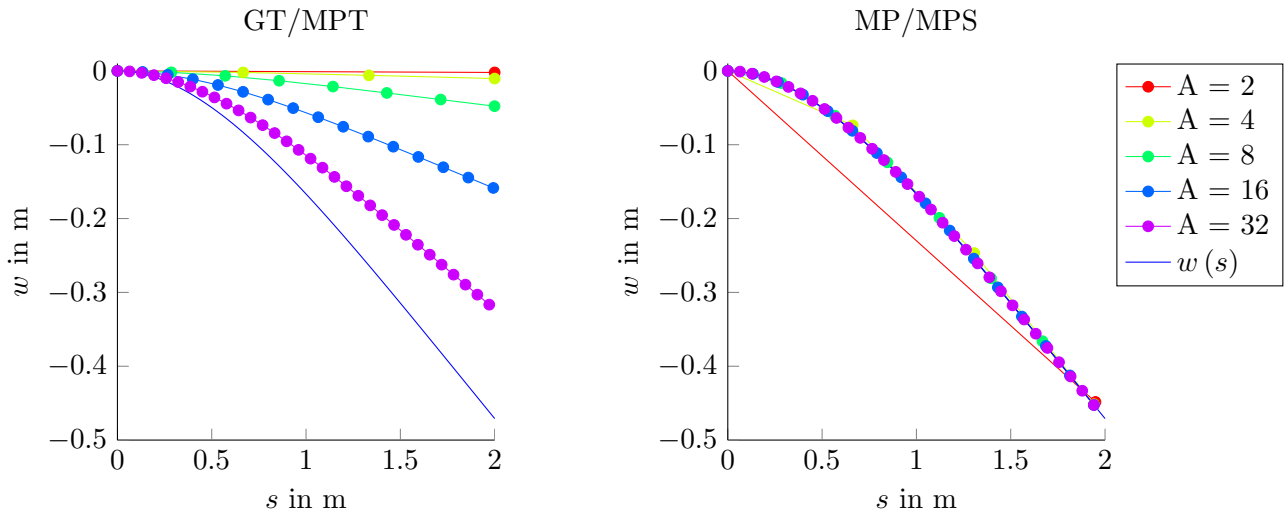

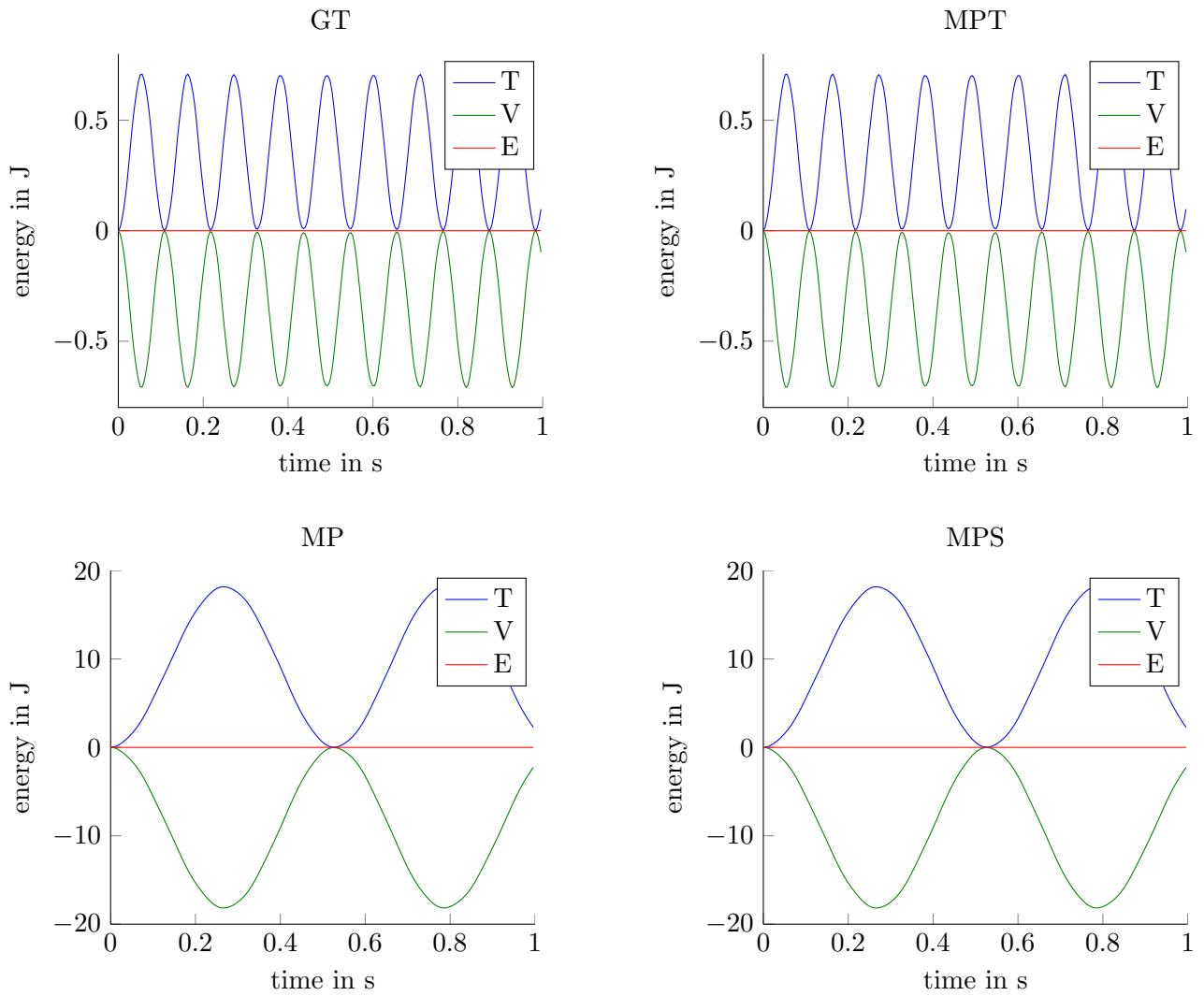Figure 2: Bending line for the quadrature rules GT/MPT and MP/MPS.

Figure 3: Energy plots of the dynamic simulation for the quadrature rules GT, MPT, MP and MPS.
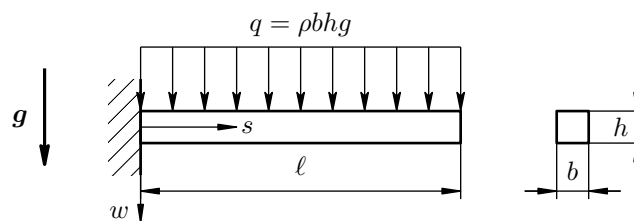

Figure 4: Beam with fixed bearing under load caused by its own weight and gravity.

References

[1] T. Leitz, S. Ober-Blöbaum, and S. Leyendecker. *Variational integrators for dynamical systems with rotational degrees of freedom.* In 11th World Congress on Computational Mechanics (WCCM XI), pp. 3148-3159, Barcelona, Spain, 2014.

[2] J.E. Marsden, and M. West. *Discrete mechanics and variational integrators.* Acta Numerica, pp. 357-514, 2001.

Relaxing mixed integer optimal control problems using a time transformation

Maik Ringkamp, Sina Ober-Blöbaum, Sigrid Leyendecker

Nonlinear control systems with instantly changing dynamic behavior can be described by differential equations $\dot{x} = F(x, u, v)$ that depend on an integer valued control function $v \in \mathcal{L}^\infty(I, \mathcal{V})$, mapping the time interval $I = [t_0, t_f]$ to the integer values $\mathcal{V} = \{1, \ldots, n_\mathcal{V}\}$. Such systems occur for example in the optimal control of a driving car with different gears [1], or a subway ride with different operation modes [2], leading to a mixed integer optimal control problem (MIOCP). A discretize-then-optimize approach leads to a mixed integer optimization problem (MIOP) that is not differentiable with respect to the integer variables, such that gradient based optimization methods can not be applied. Differentiability with respect to all optimization variables can be achieved by reformulating the MIOCP, e.g. by using a relaxed binary control function [2], or by introducing a fixed integer control function $\bar{v}_{N,n} \in \mathcal{L}^\infty(I, \mathcal{V})$ and a time transformation t_w that allows to partially deactivate the fixed integer control function [1]. The latter approach is presented here, while the main focus lies on new theoretical and numerical results that take different functions $\bar{v}_{N,n}$ into account. The time interval I is partitioned into N major intervals I_j and each $I_j = [t_{j-1}, t_j[$ into n minor intervals $I_j^i = [\tau_j^{i-1}, \tau_j^i[$. Then, the function $\bar{v}_{N,n}$ is defined to be constant on each minor interval I_j^i. Figure 1 depicts an example of such a fixed integer control function.
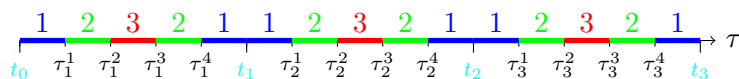
Figure 1: Example of a fixed integer control function $\bar{v}_{N,n}$ with $\mathcal{V} = \{1, 2, 3\}$ and $N = 3$ major and $n = 5$ minor intervals.

The depicted function is called *consistent* to every integer control function v, because a switch of v at any time in a major interval I_j from a value $l_1 \in \mathcal{V}$ to a value $l_2 \in \mathcal{V}$ can be achieved with $\bar{v}_{N,n}$ by scaling the minor intervals I_j^i, in particular some minor intervals can be deactivated by scaling to zero. The scaling is accomplished by a time transformation $t_w \in \mathcal{W}^{1,\infty}(I, I)$ resulting from a time control $w \in \mathcal{L}^\infty(I, \mathbb{R})$ with $\Delta I_j = \int_{I_j} w(s)ds$ and $w(\tau) \geq 0$ for a.e. $\tau \in I$. The time transformation with derivative $t_w' = \frac{dt_w}{d\tau}(\tau) = w(\tau)$ for a.e. $\tau \in I$ is defined by

$$t_w(\tau) := t_0 + \int_{t_0}^{\tau} w(s)ds, \tag{1}$$

and assures that the mapping of a major interval is surjective $t_w(I_j) = I_j$ even if several minor intervals I_j^i are deactivated, i.e. $t_w(I_j^i)$ has zero length. Then, the time transformed MIOCP is defined as follows:

Definition 1 *(TMIOCP)*

$$\min_{x,u,w} \quad J^*(x, u, w) = \int_I w(\tau) B(x(\tau), u(\tau), \bar{v}_{N,n}(\tau))\, d\tau \tag{2}$$

$$\text{s. t.} \quad \dot{x}(\tau) = w(\tau) F(x(\tau), u(\tau), \bar{v}_{N,n}(\tau)) \qquad \text{for a.e. } \tau \in I \tag{3}$$

$$g_0(x(\tau), u(\tau)) \leq 0 \qquad \text{for a.e. } \tau \in I \tag{4}$$

$$w(\tau) g(x(\tau), u(\tau), \bar{v}_{N,n}(\tau)) \leq 0 \qquad \text{for a.e. } \tau \in I \tag{5}$$

$$r(x(t_0), x(t_N)) = 0 \tag{6}$$

$$w(\tau) \geq 0 \qquad \text{for a.e. } \tau \in I \tag{7}$$

$$\Delta I_j = \int_{I_j} w(s)\, ds \tag{8}$$

hybrid mass oscillator $\qquad J^*(u) = 6.0520911696 \cdot 10^{-11} \qquad J^*(u) = 3.7453160945 \cdot 10^8$
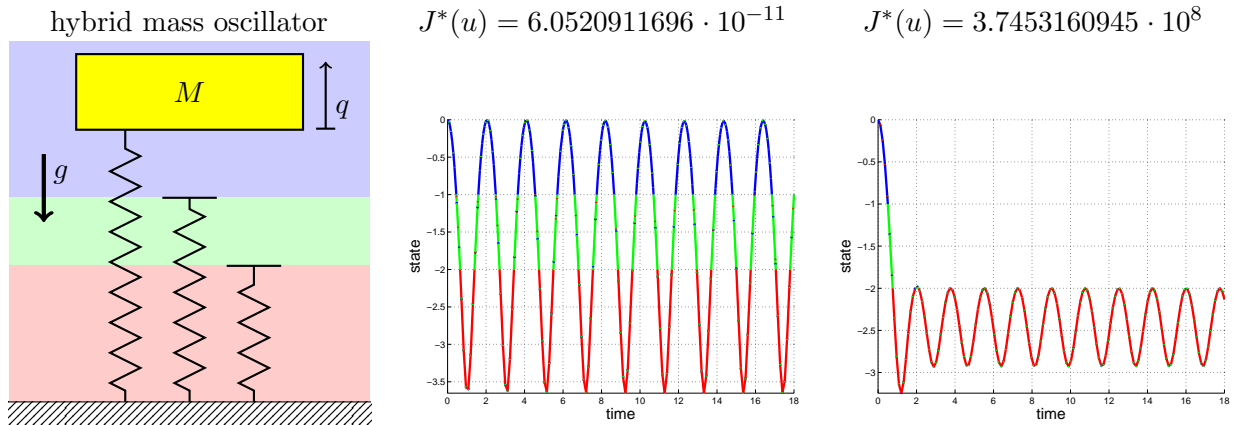
Figure 2: Sketch of the hybrid mass oscillator (left). Locally optimal discretized state trajectory of the hybrid mass oscillator in the CC case (middle) and in the NCC case (right).

Here, J is the objective functional, g_0 and g are inequality constraints and r represents the boundary conditions. An example demonstrates that solving a TMIOCP using a control consistent (CC) fixed integer control function $\bar{v}_{N,n}$ can lead to a lower number of discretization variables as a TMIOCP that utilizes a fixed integer function that is not control consistent (NCC). The number of necessary discretization variables depends on the total number of used minor intervals and it is shown that the total number can be unbounded in the NCC case and is bounded in the CC case, even though the number of minor intervals for each major interval is lower in the NCC case. As a numerical example, a hybrid mass oscillator is considered (Figure 2 (left)), that extends the example given in [3] to three springs. The springs are mounted in parallel and relaxed in different positions. A mass is fixed on the first spring, and the second and third springs are activated and deactivated depending on the position of the mass. A minimization with unspecified end position results in the CC case in the expected oscillating trajectory with almost no control effort. In contrast, the locally optimal trajectory in the NCC case avoids specific switches in the interior of major intervals by oscillating with a low amplitude and needs a high control effort. The state trajectories are plotted in Figure 2 (middle) and (right). An extension to bipedal walking models is planed in future works.

References

[1]   M. Gerdts. *A variable time transformation method for mixed-integer optimal control problems.* Optimal Control Applications and Methods, Vol. 27, No. 3, pp. 169–182, 2006.

[2]   S. Sager, H. G. Bock, G. Reinelt. *Direct methods with maximal lower bound for mixed-integer optimal control problems.* Mathematical Programming, Vol. 118, No. 1, pp. 109–149, 2009.

[3]   K. Flaßkamp, S. Ober-Blöbaum. *Variational Formulation and Optimal Control of Hybrid Lagrangian Systems.* Proceedings of the 14th international conference on Hybrid systems: Computation and Control, pp. 241–250, Chicago, Illinois, 2011.

Viscoelastic finite element modelling of dielectric elastomers

Tristan Schlögl, Sigrid Leyendecker

Modern robotic systems suffer some severe dynamic limitations. The rigid coupling between electrical drives and joints does not allow for dynamic motions like they occur in nature, where muscles act as an energy buffer and store energy. However, this elastic behaviour plays an important role when considering humanoid systems in terms of safety, energy efficiency and robustness. Stacked dielectric elastomer actuators are composed of a series of elastic capacitors. Each capacitor consists of two conductive layers separated by an insulating material.. In this collaborative work a dielectric silicone is used as the main component and conductive layers are introduced by adding carbon nanotubes. The structure of a single actuator cell is illustrated in Figure 1 on the left hand side. As with capacitors, when an external voltage is applied to the conductive layers, an electric field is established. To be observed in Figure 1 on the right hand side, the electric field leads to polarisation. Attracting bound charges then induce a contraction of the silicone. Due to its similarity with real muscles, dielectric actuators are also known as artificial muscles.
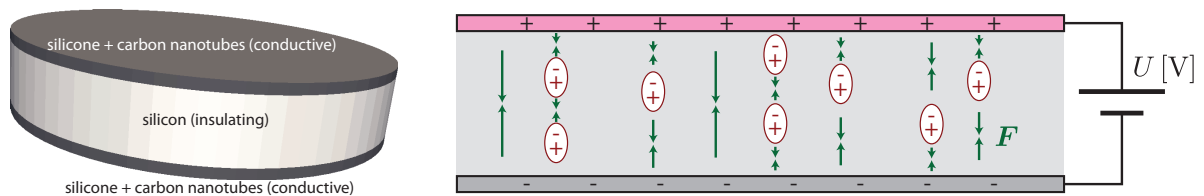
Figure 1: Three layer structure of a dielectric elastomer actuator (left) and its functional principle (right).

The functional principle can be described by the Maxwell equations, the balance of momentum and constitutive material laws. It is assumed that the electric field $\boldsymbol{E}$ can be regarded as quasi-static, no external magnetic fields are applied and no free currents and electric charges are present. Electrostatics are then covered by

$$\nabla_{\boldsymbol{X}} \times \boldsymbol{E} = \boldsymbol{0} \qquad \text{and} \qquad \nabla_{\boldsymbol{X}} \cdot \boldsymbol{D} = 0, \tag{1}$$

with the electric displacement vector $\boldsymbol{D}$ and $\boldsymbol{X}$ being a material point in the reference configuration. Note that additional boundary terms are needed in order to solve the equations. Vectors in the reference configuration are obtained by the pull-back operations $\boldsymbol{E} = \boldsymbol{F}^T \cdot \boldsymbol{e}$ and $\boldsymbol{D} = J\boldsymbol{F}^{-1} \cdot \boldsymbol{d}$ for the electric field $\boldsymbol{e}$ and the electric displacement $\boldsymbol{d}$ in the spatial configuration, using the deformation gradient $\boldsymbol{F}$ and its determinant $J = \det(\boldsymbol{F})$. The balance of momentum is given by

$$\nabla_{\boldsymbol{X}} \cdot \boldsymbol{P} + \boldsymbol{f}_e = \rho_0 \ddot{\boldsymbol{x}}, \tag{2}$$

where $\boldsymbol{P}$ is the Piola-Kirchhoff stress tensor, $\boldsymbol{f}_e$ is the volume force resulting from electrostatics, ρ_0 is the mass density in the reference configuration and $\ddot{\boldsymbol{x}}$ is the absolute acceleration of a spatial point. In analogy to the Kelvin-Voigt model where the total force is split into the sum of an elastic and a viscous part, the stress tensor is split into a conservative elastic part and a time dependent viscous part as

$$\boldsymbol{P}(\boldsymbol{F}, \dot{\boldsymbol{F}}) = \boldsymbol{P}^{\mathrm{ela}}(\boldsymbol{F}) + \boldsymbol{P}^{\mathrm{vis}}(\boldsymbol{F}, \dot{\boldsymbol{F}}). \tag{3}$$

Coupled by the electrostatic body force

$$\boldsymbol{f}_e = \nabla_X \left(\boldsymbol{F}^{-T} \cdot \boldsymbol{E} \right) \cdot \boldsymbol{P}^{\mathrm{el}}, \tag{4}$$

with the material polarisation vector $\boldsymbol{P}^{\mathrm{el}}$, see [2], after some calculation Equation (2) can be rewritten as

$$\nabla_X \cdot \boldsymbol{T} = \rho_0 \ddot{\boldsymbol{x}}, \tag{5}$$

with the total stress $\boldsymbol{T}$ being superposed of $\boldsymbol{P}$ and some electric counterpart. Note that for an actual simulation, Equation (5) needs to be completed by initial and boundary conditions.

In order to discretise the coupled problem using finite elements and symplectic time integration, a variational formulation is derived. The Lagrangian is composed of the kinetic energy and the potential energy density function

$$\Omega(\boldsymbol{F}, \boldsymbol{E}) = \underbrace{\frac{\mu}{2}[\boldsymbol{C} : \boldsymbol{1} - 3] - \mu \ln(J) + \frac{\lambda}{2}[\ln(J)]^2}_{\text{Neo-Hooke}} + \underbrace{c_1 \boldsymbol{E} \cdot \boldsymbol{E}}_{\text{electric}} + \underbrace{c_2 \boldsymbol{C} : [\boldsymbol{E} \otimes \boldsymbol{E}]}_{\text{coupling}} - \underbrace{\frac{1}{2} \varepsilon_0 J \boldsymbol{C}^{-1} : [\boldsymbol{E} \otimes \boldsymbol{E}]}_{\text{free space}} \tag{6}$$

with Lamé parameters μ and λ, electrical parameters c_1 and c_2, the right Cauchy-Green tensor $\boldsymbol{C} = \boldsymbol{F}^T \cdot \boldsymbol{F}$ and the rank two identity $\boldsymbol{1}$, see [3]. The Lagrange d'Alembert principle with non-conservative contributions that account for viscous terms then leads to a variational setting of the coupled problem. The action integral is approximated using quadrature rules. Hexahedral finite elements with linear shape functions are used for the spatial discretisation and finite differences are used for the temporal discretisation. The Lagrange d'Alembert principle is applied to the discrete set of equations, resulting in a non-linear variational integration scheme [1]. Variational integration guarantees that important characteristics of the system are preserved exactly. Using a Newton-Raphson scheme and providing initial values and boundary conditions, the non-linear coupled problem can be solved for unknown displacements and electric potentials at each finite element node.
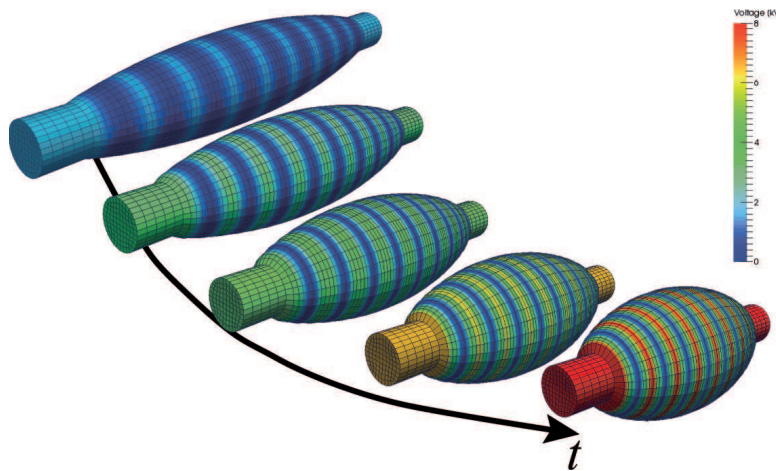

Figure 2: Contraction of a dielectric elastomer actuator in muscle shape due to an applied voltage.

Figure 2 illustrates the results of an in-house MATLAB FEM solver, evaluating the quasi-static states of a given muscle shape for increasing voltage. As the muscle is not mechanically fixed, the applied voltage leads to a contraction in direction of the electric field. At the same time, the cross section area of the muscle expands because the silicone is incompressible. Different damping intensities are studied using a three-dimensional extension of the Kelvin-Voigt model

$$\boldsymbol{P}^{\mathrm{vis}}(\boldsymbol{F}, \dot{\boldsymbol{F}}) = \frac{1}{2} J \eta \left[\boldsymbol{F}^{-T} \cdot \dot{\boldsymbol{F}}^T \cdot \boldsymbol{F}^{-T} + \dot{\boldsymbol{F}} \cdot \boldsymbol{C}^{-1} \right], \tag{7}$$

with the damping parameter η, see [4]. The parameter is varied in a range from 0 to $0.1 \frac{\mathrm{g}}{\mathrm{ms\,mm}}$. The illustrating geometry is a unit cube of the dielectric elastomer material with an edge length of $2\,\mathrm{mm}$ and its centre placed in the origin of the global coordinate system, as shown in Figure 3 on the left hand side. Essential boundary conditions are applied as follows. Translational symmetry boundary constraints on all rear faces in the view of Figure 3 eliminate rigid body motions. The bottom face is fixed to ground potential. The left half of the upper face is loaded with $20\,\mathrm{kV}$. On the right hand side of the figure, the total energy of the cube is plotted over time. Increasing the damping parameter η results in decreasing oscillations until the critical damping is reached (approximately $\eta = 0.05 \frac{\mathrm{g}}{\mathrm{ms\,mm}}$). Further increase of η leads to a growing total time that is needed for reaching the steady state.
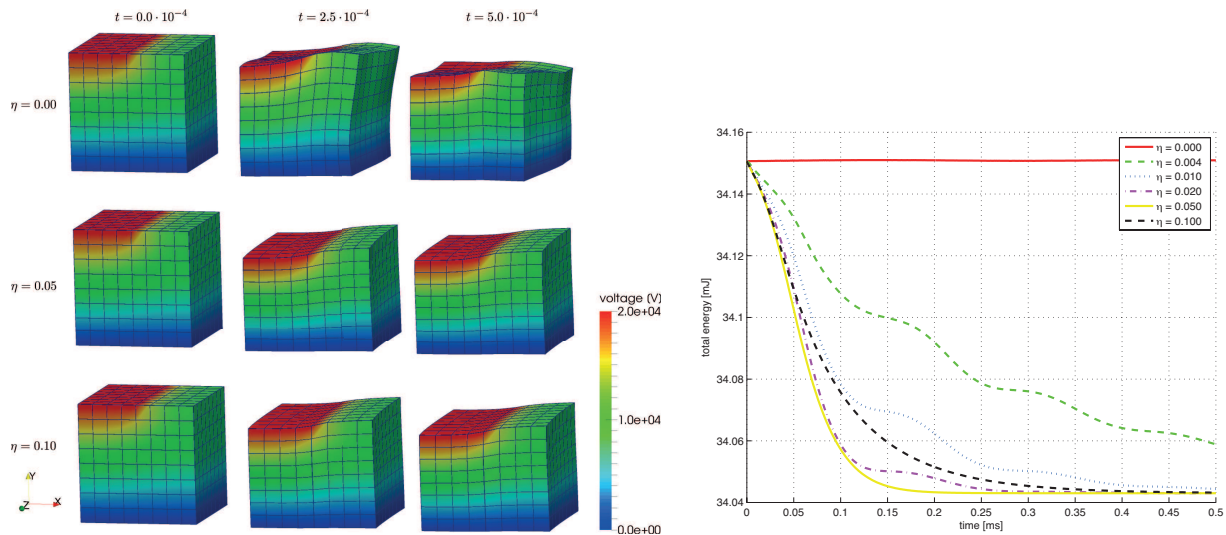
Figure 3: Time dependent state (left) and energy behaviour (right) of the dielectric elastomer material for different damping parameters.

The presented model for electrostatic-viscoelastic coupling forms the basis for future work regarding optimal control problems, where DEAs are used as actuators in robotics.

References

[1] S. Leyendecker, J.E. Marsden, and M. Ortiz. *Variational integrators for constrained dynamical systems.* Z. Angew. Math. Mech., Vol. 88, pp. 677-708, 2008.

[2] Y.H. Pao. *Electromagnetic forces in deformable continua.* Mechanics Today, Vol. 4, pp. 209-306, 1978.

[3] D.K. Vu, P. Steinmann, and G. Possart. *Numerical modelling of non-linear electroelasticity.* International Journal for Numerical Methods in Engineering, Vol. 70, pp. 685-704, 2006.

[4] P. Wriggers. *Nonlinear Finite Element Methods.* Springer, 2008.

4 Activities

4.1 Teaching

Wintersemester 2014/2015

Biomechanik der Bewegung (MT)
    Vorlesung + Übung   H. Lang

Dynamik starrer Körper (MB, ME, WING, IP, BPT, CE)
    Vorlesung   S. Leyendecker
    Übung + Tutorium   T. Gail, T. Leitz
                                                        M. Ringkamp, T. Schlögl

Mehrkörperdynamik (MB, ME, WING, TM, BPT)
    Vorlesung   S. Leyendecker
    Übung   O.T. Kosmas

Numerische Methoden in der Mechanik (MB, ME, WING, TM, BPT)
    Vorlesung + Übung   H. Lang, D. Budday

Theoretische Dynamik I (MB, ME, WING, TM, BPT)
    Vorlesung + Übung   H. Lang

Sommersemester 2014

Biomechanik (MT, MA, GPP)
    Vorlesung + Übung   H. Lang
    geprüft   52 + 16 (WS 13/14)

Dynamik nichtlinearer Balken (MB, M, Ph, CE, ME, WING)
    Vorlesung + Übung   H. Lang, D. Budday

    geprüft   4

Geometrische numerische Integration (MB, ME, WING, BPT)
    Vorlesung   S. Leyendecker
    Übung   H. Lang
    geprüft   3 + 1 (WS 14/15)

Statik und Festigkeitslehre
(CBI, CE, ET, LSE, ME, MWT, IP, MT, CEN, BPT)
    Vorlesung   S. Leyendecker
    Übung + Tutorium   T. Gail, N. Bach
                                                     D. Budday, O.T. Kosmas
                                                       T. Leitz, M. Ringkamp
    geprüft   519

Theoretische Dynamik II
(M, TM, MB, ME, CE, BPT, WING, Ph)
    Vorlesung + Übung   H. Lang
    geprüft   9 + 1 (WS 13/14)

Rechnerunterstützte Produktentwicklung (RPE)
Versuch 6: Mehrkörpersimulation in Simulink
    (MB, ME, WING) Praktikum   T. Gail, O.T. Kosmas
                                       T. Leitz, M. Ringkamp, T. Schlögl

    Teilnehmer   62

Wintersemester 2013/2014

Biomechanik der Bewegung (MT)
    Vorlesung + Übung   H. Lang
    geprüft   34 + 4 (SS 2014)

Dynamik starrer Körper (MB, ME, WING, IP, BPT, CE)
    Vorlesung   S. Leyendecker
    Übung + Tutorium   N. Bach, T. Leitz
                                       O.T. Kosmas, M. Ringkamp
                                               T. Schlögl
    geprüft   427 + 142 (SS 2014)

Mehrkörperdynamik (MB, ME, WING, TM, BPT, CE)
    Vorlesung   S. Leyendecker
    Übung   H. Lang
    geprüft   46 + 10 (SS 2014)

Numerische Methoden in der Mechanik (MB, ME, WING, TM, CE, BPT)
    Vorlesung + Übung   H. Lang
    geprüft   26 + 7 (SS 2014)

Theoretische Dynamik I (MB, ME, WING, TM, BPT)
    Vorlesung + Übung   H. Lang
    geprüft   19 + 6 (SS 2014)

4.2 Theses

PhD theses

- Ramona Maas
  Biomechanics and optimal control simulations of the human upper extremity

Project theses

- Hannah Laube
  Schubweicher Reissner- und Kirchhoff-Balken: Modellvergleich und numerischer Aufwand bei der Zeitintegration

- Theresa Wenger
  Variationelle Integratoren höherer Ordnung für dynamische Systeme mit Zwangsbedingungen

- Fabian Zimber
  Dynamics of a robotic manipulator using closed loop Inverse kinematic and dynamic algorithms

Bachelor theses

- Lukas Allabar
  Structure preserving simulation of a planar slider crank with translational joint clearance

- Lukas Erdt
  Variational integration methods for the Fermi-Pasta-Uiam problem

- Lisa Machata
  Mechanical testing of transtibial foot protheses with regard to energy release and deformation behaviour

- Magdalena Roether
  Modellierung eines menschlichen Femurs unter statischer Belastung mittels Cosserat-Modell und Vergleich mit linearem Modell

- Benedikt Rohrmüller
  Modellbildung und Simulation spurgebundener Autorennbahnen

- Manuel Roppelt
  Implementation of discontinuous variational time integrators for many particle collisions

- Sabine Weingärtner
  Untersuchung der Kinematik der Stewart-Plattform als externer Fixateur

4.3 Seminar for Mechanics

together with the Chair of Applied Mechanics LTM

13.01.2014   Jorge Ambrósio
IDME/IST – Instituto Superior Técnico, Lisboa, Portugal
Multibody dynamics methodologies with applications to biomechanics and vehicle dynamics

10.02.2014   Veronika Kräck
Chair of Electrical Drives and Machines, FAU Erlangen-Nuremberg, Germany
Blockstrukturierte Finite-Difference-Time-Domain (FDTD) Methode zur Berechnung dreidimensionaler niederfrequenter elektromagnetischer Feldprobleme

12.02.2014   Michael Wolff
ZeTeM, University of Bremen, Germany
On modeling of continuous bodies with singular sharp interfaces

12.02.2014   Cristian G. Gebhardt
IWES, Bremerhaven, Germany
Fluid-structure interaction of mechanical systems immersed in low-subsonic flows: the wind turbine case

13.02.2014   Mykola Tkachuk
National Technical University, Kharkiv, Ukraine
On modeling of continous bodies with singular sharp interfaces

31.03.2014   Andreas Müller
University of Michigan-Shanghai Jiao Tong, China
Anwendung der Schraubentheorie in der Mehrkörperdynamik

14.05.2014   Markus Breitfuss
Institute of Technical Mechanics, Johannes Kepler Universität Linz, Austria
DEIM for the efficient computation of contact interface stresses

02.06.2014   Jean-Paul Pelteret
Chair of Applied Mechanics, FAU Erlangen-Nuremberg, Germany
A computational neuromuscular model of the human upper airway

18.06.2014   Dominik Kern
TU Chemnitz, Germany
Variational integrators for thermoviscoelastic coupled dynamic systems with heat conduction

20.06.2014   Henry van den Bedem
Stanford University, SLAC National Accelerator Laboratory, USA
Molecular-scale kinematics in computational structural biology

30.06.2014   Masato Tanaka
              Toyota Central R&D Labs., Inc., Japan
              Implementation of material modeling approaches at finite strains using a highly accurate numerical derivative scheme

07.07.2014   Mohd Shariff
              Department of Applied Mathematics and Science, Khalifa University of Science, Technology and Research, Israel
              Principal axis formulations in anisotropic solid mechanics

07.07.2014   Manish Vasoya
              Institut Jean Le Rond dAlembert, CNRS, Paris, France
              Propagation of tensile planar cracks in heterogeneous media

19.09.2014   Manuel Roppelt
              Bachelor thesis, Chair of Applied Dynamics, University of Erlangen-Nuremberg
              Implementation of discontinuous variational time integrators for many particle collisions

24.10.2014   Lisa Machata
              Bachelor thesis, Chair of Applied Dynamics, University of Erlangen-Nuremberg
              Mechanical testing of transtibial foot protheses with regard to energy release and deformation behaviour

17.11.2014   Theresa Wenger
              Project thesis, Chair of Applied Dynamics, University of Erlangen-Nuremberg
              Variationelle Integratoren höherer Ordnung für dynamische Systeme mit Zwangsbedingungen

01.12.2014   Benedikt Rohrmüller
              Bachelor thesis, Chair of Applied Dynamics, University of Erlangen-Nuremberg
              Modellbildung und Simulation spurgebundener Autorennbahnen

03.12.2014   Fabian Zimber
              Project thesis, Chair of Applied Dynamics, University of Erlangen-Nuremberg
              Dynamics of a robotic manipulator using closed loop Inverse kinematic and dynamic algorithms

04.12.2014   Debora Clever
              IWR, ORB, University of Heidelberg, Germany
              Optimization in robotics and biomechanics with focus on human and humanoid locomotion
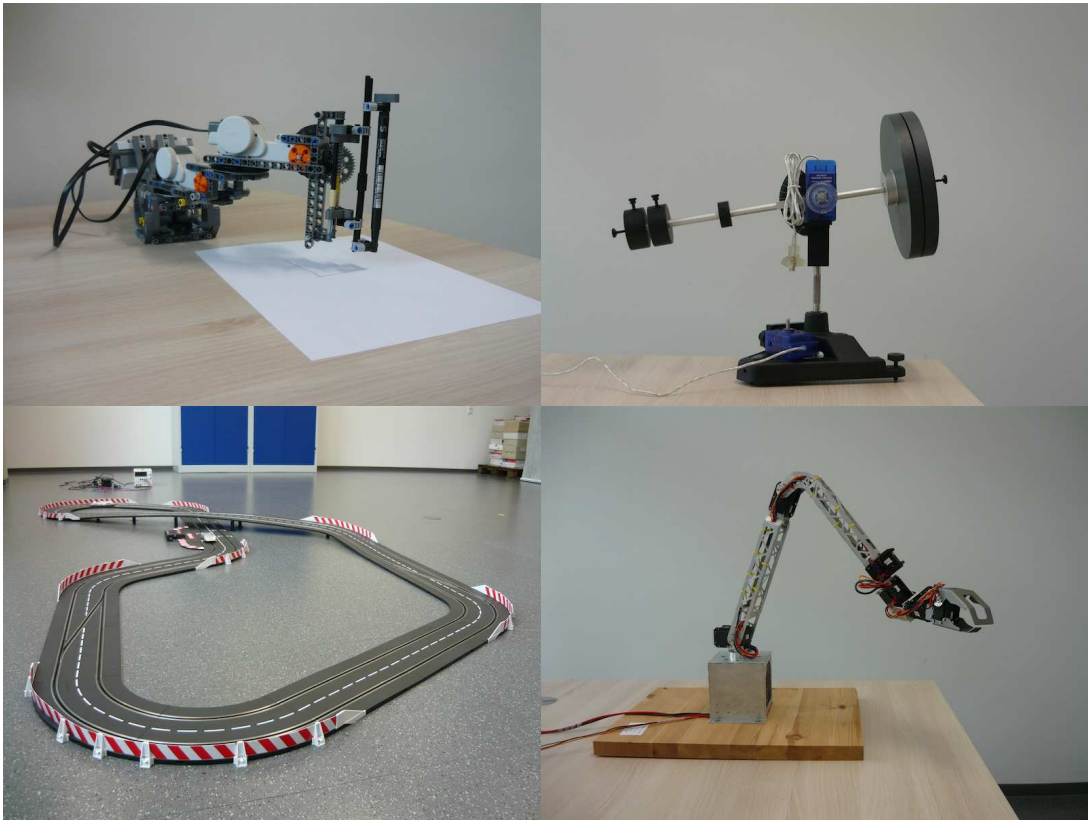
4.4 Dynamics laboratory

Figure 1: Some of the lab course experiments.

The LTD is in the progress of setting up a dynamics laboratory for teaching purposes. First beginnings were already made in 2013 and it is gradually taking shape. Within the last year, a number of experiments has been added and developed. By now, there is an inverted pendulum actuated by a robot with two linear degrees of freedom and a robot with six degrees of freedom to investigate optimised trajectories. In addition two experiments with LEGO MINDSTORMS have been prepared and tested. One of them is a SCARA robot which gives an introduction to kinematics and inverse kinematics of robots and the question of accuracy can be investigated. The other one is a selfbalancing robot with which changes in the Simulink control model or the hardware are examined. Further, a slot car track is present. So far, one student has written a bachelor thesis on modeling and simulating the dynamics of a slot car on the track. To reach the desired state of applying optimal control theory to the slot car track, several more student projects will be assigned. Futhermore, a ball balancer is in preperation to illustrate closed loop control. A one dimensional and a two dimensional version are planned. Supplementary, two complete experiments are a gyroscope to demonstrate the conservation of angular momentum and to study precession and nutation, and secondly, a set of coupled pendula which can be used to show overlapping frequenzy fluctuation. Moreover, an Atwood machine is planned to point out basic laws of dynamics and to measure gravitational acceleration. Even though there has been great progress during 2014, a lot of things remain to be prepared before the dynamics lab takes place with students for the first time.

4.5 Summer schools

Singular Configurations of Mechanisms and Manipulators
(16-20 September 2014)

Dominik Budday participated in this CISM course in Udine, Italy. The course was organized by Dimiter Zlatanov and Andreas Müller and held at the lecture room at CISM. Dimiter Zlatanov, Manfred Husty, Oriol Bohigas, Philippe Wenger and Andreas Müller gave lectures on various singularity related topics, including classification of singularities, analytical and numerical computation of the singularity set, geometric aspects and applications to mechanisms and robotics. Participants could exchange their ideas and discuss research projects with each other and the lecturers in between talks. The group was a great mix of different backgrounds and research topics and engaged in self-organized after hours social events throughout the week. Udine was a great location for this very informative and exciting summer school.

4.6 Press releases

Alexander – aktuelles aus der Friedrich-Alexander-Universität Nr. 96, October 2014

Wollen Roboter mit künstlichen Muskeln ausstatten: Tristan Schlögl (l.) und Sebastian Reitelshöfer. Im kleinen Bild zu sehen: ein erster Prototyp einer Muskelzelle. Wird Spannung auf ihn angelegt, zieht sich die Muskelzelle zusammen und der Querschnitt vergrößert sich.

Muskeln statt Motor

FAU-Forscher entwickeln künstliche Muskeln für Roboter

Sie laufen, tanzen und arbeiten sogar Seite an Seite mit Menschen zusammen: Humanoide Roboter bewegen sich inzwischen ähnlich wie Menschen. Aber: „Die Bewegungen von humanoiden Robotern sind fernab von dem, was ein natürliches System kann", sagt Sebastian Reitelshöfer, wissenschaftlicher Mitarbeiter am Lehrstuhl für Fertigungsautomatisierung und Produktionssystematik (FAPS). Der Grund: Wo der Mensch Muskeln nutzt, stehen den Robotern nur Elektromotoren zur Verfügung. Dadurch können humanoide Roboter Bewegungen bisher weder dämpfen noch abfedern, können nicht flexibel reagieren. Um das zu ändern, wollen Sebastian Reitelshöfer und sein Kollege Tristan Schlögl Roboter mit künstlichen Muskeln ausstatten.

Vorbild Mensch

Die Robotermuskeln bestehen aus speziell entwickelten Kunststoffstrukturen, die sich durch elektrische Spannung zusammenziehen, also ähnlich menschlichen Muskeln kontrahieren. Aufgebaut sind die Muskeln aus mehreren Schichten. Eine Schicht besteht aus leitfähigen Silikonlagen, die durch eine isolierende Silikonschicht getrennt sind.

Wird elektrische Spannung zugeführt, zieht sich das Material zusammen, wodurch sich der Querschnitt vergrößert. Rund 10.000 Schichten benötigt ein einziger Muskel. „Die Schichten müssen dementsprechend sehr dünn sein und sie müssen gut zusammenhalten", erklärt Reitelshöfer. Am FAPS forschen er und seine Kollegen, wie sie die Schichten am besten mit einem 3D-Drucker serienmäßig herstellen können.

Ist der Produktionsprozess geklärt, stellt sich die nächste Frage: Wie können die künstlichen Muskeln gezielt gesteuert werden? Daran forscht Tristan Schlögl vom Lehrstuhl für Technische Dynamik. Am Computer simuliert er, welche Spannung zu welchem Zeitpunkt auf die Muskeln angewendet werden muss, damit dieser die gewünschte Bewegung ausführt. Und das mit einigem Aufwand: „Bisher wurden für solche Simulationen meist vereinfachte Modelle verwendet. Die waren aber ungenau. In diesem Projekt beschreiben wir die grundlegenden Ebenen", erklärt Schlögl.

Noch stehen Reitelshöfer und Schlögl am Anfang ihrer Forschungen, mit einem aus wenigen Lagen bestehenden Prototyp ihres künstlichen Muskels rechnen die beiden aber bis zum Jahr 2015. ■ *kp*

Handelszeitung Switzerland, Nr. 2, 2015

Die Natur der Dinge

Bionik Unternehmen schauen sich Hightech-Lösungen für ihre Produkte von der Pflanzen- und Tierwelt ab.

JAN VOLLMER

Damals, im Jahr 1941, geht der Ingenieur George de Mestral in den Schweizer Bergen spazieren. Kletten bleiben an seiner Kleidung und im Fell seines Hundes hängen. De Mestral ist ein neugieriger, verspielter Typ. Schon als Junge soll er versucht haben, ein mit Stoff bespanntes Modellbauflugzeug patentieren zu lassen. Er legt die Kletten unter ein Mikroskop und entdeckt die kleinen elastischen Haken an den Enden der vermeintlichen Stacheln. De Mestral ist von den Kletten fasziniert und webt selbst ein Band mit Haken. Zehn Jahre später, im Jahr 1951, gründet er die Firma Velcro und produziert den ersten Klettverschluss der Welt in Serie. George de Mestral war einer der ersten und erfolgreichsten Schweizer Bioniker – ein Ingenieur, der sich für seine Lösungen von der Natur inspirieren liess.

Regine Schwilch hat mit dem Ingenieur de Mestral mehr gemeinsam, als ihr lieb ist. Die Biologin aus Luzern sucht mit ihrer Firma evosolutions auch in der Natur nach Lösungsansätzen für die Industrie. Und wie de Mestral ist sie als Bionikerin ziemlich alleine auf weiter Flur, zumindest in der Schweiz.

Bei einem ihrer Projekte ahmte sie die Flossen eines Buckelwals für die Finne eines Surfboards nach. Die Flossen eines Buckelwals sind an der Oberseite gezackt und machen ihn dank ihrer Strömungsdynamik zu einem der wendigsten Wale. Regine Schwilch hat daraufhin die Finne eines Surfbretts gezackt und sie somit stabiler für Wenden gemacht. «Meine Leistung ist es, eine Problemstellung neu zu betrachten und nach einem bionischen Weg zu suchen», erklärt Schwilch. «Ein Kunde kam etwa mit einer sich drehenden Achse zu mir, die er nicht hundertprozentig dicht bekommen hat. Aber auch die Natur ist selten ganz dicht. Ich habe ihn dann beraten, wie er mit einem konstanten Leakage umgehen kann», erklärt Schwilch.

Ein anderes Beispiel: Die Firma V-Zug hat nach neuen Filtersystemen für Geschirrspülmaschinen gesucht. «Wir haben dort einen Filter entwickelt, der das Wasser nicht wie üblich beim Durchlaufen filtert.

Enten und Flamingos filtrieren ihre Nahrung aus dem Wasser, indem sie Wasser in den Schnabel aufnehmen und zwischen den geschlossenen Schnabelrändern durch eine Siebstruktur wieder ausströmen lassen. Mittlerweile haben wir dazu auch ein Patent eingereicht», erzählt Schwilch.

Schweizer Pioniere

Neben Regine Schwilch gehört auch Daniel Portmann zu der kleinen Truppe, die sich in der Schweiz für Bionik stark macht. Vor fünf Jahren gründete der Betriebs- und Produktionsingenieur das Bionik-Zentrum Luzern, das interessierten Unternehmen natürliche Lösungen nahebringt. Dass die Schweiz damals noch nicht so viel mit Bionik am Hut hatte, mag letztendlich auch an der Schweizer Topografie liegen: «Die absoluten Ursprünge der Technik kamen von der amerikanischen Navy», erklärt Portmann. «Man wollte wissen, wie man Torpedos nach tierischem Vorbild verbessern kann – und Torpedos brauchten wir in der Schweiz natürlich nicht.»

Bionik sei nichts, was die in Sachen Innovation ohnehin gut aufgestellte Schweiz völlig umkremple, so Portmann. Eher ein Werkzeug, um Ideen zu recherchieren.

Wie bionische Forschung in der Industrie aussehen kann, zeigt beispielsweise der süddeutsche Maschinenbauer Festo. Auf die letzten Messen nahm der Automatisierungsriese auch ein pneumatisch hüpfendes Känguru mit. Das besondere an diesem Elektro-Känguru ist allerdings nicht, dass eine Maschine so aussieht wie ein Tier, sondern die Technik, mit der es sich bewegt: «Die effiziente Fortbewegungsart eines Kängurus gilt als einzigartig in der Tierwelt», sagt Heinrich Frontzek von Festo. «Die Hinterbeine wirken wie ein Federelement, welches die Energie aus einem Sprung auf den nächsten transferiert. Sobald ein Känguru zu hüpfen beginnt, kann es seine Geschwindigkeit erhöhen, ohne gleichzeitig den Energieverbrauch zu erhöhen.»

Bei dem elektronischen Känguru hat Festo dieses Funktionsprinzip mit einer Feder anstelle einer Sehne und einer Druckluftkammer nachgebaut. Natürlich will der Automatisierungstechniker nicht in den Markt für elektrische Kängurus einsteigen. Aber im Unternehmen ist dank dem Projekt Know-how vorhanden, «wie pneumatische und elektrische Antriebstechnik intelligent in einem hochdynamischen System kombiniert werden», so Heinrich Frontzek.

Känguru als Vorbild

Professorin Sigrid Leyendecker von der Universität Erlangen-Nürnberg hüpft dabei noch einen Schritt weiter: Leyendecker forscht an einem neuen Antrieb – Aktor genannt –, der die Funktionsweise von Muskeln nachahmt. Sie berechnet in numerischen Simulationen, wie ein Gewebe aus Silikon und Carbon Nano Tubes sich unter elektrischer Spannung zusammenziehen und dehnen würde, wie echte Muskeln. Es geht darum, die Antriebstechniken weicher und flexibler zu machen. Künstliche Muskeln hätten aber etliche andere Vorteile gegenüber herkömmlichen Antriebsarten: «Derzeitige Robotersysteme setzen nur einen geringen Prozentsatz der verbrauchten Energie tatsächlich in Bewegung um und sind relativ schwer. Ausserdem ist die Herstellung von Elektromotoren sehr energieintensiv, man braucht zum Beispiel in Permanentmagneten Ressourcen wie Seltene Erden», so Leyendecker. «Künstliche Muskeln aus Silikon hingegen wären leichter, man verspricht sich energieeffizientere Bewegung und eine ressourceneffizientere Herstellung.»

Aber nicht alles ist so futuristisch wie Festos Känguru oder die Muskeln aus Silikon: Mercedes-Benz liess sich unlängst bei einer Studie vom tropischen Kofferfisch inspirieren: «Er hat in vielerlei Hinsicht die gleichen Bedingungen wie Autos: Er muss mit seinen Kräften haushalten und sich mit geringstmöglichem Energieeinsatz fortbewegen, was starke Muskeln und eine strömungsgünstige Linie erfordert. Er muss hohem Druck standhalten und seinen Körper bei Kollisionen schützen, also eine steife Aussenhaut notwendig ist», so der Autobauer. Herausgekommen ist dabei ein Kompaktwagen, der äusserlich tatsächlich an den Kofferfisch erinnert, dessen steife Karosserie einem organischen Skelett ähnelt und der einen cW-Wert von 0,19 aufweist. Der cW-Wert ist die wissenschaftliche Grösse des Luftwiderstands, der wiederum rund 50 Prozent des Spritverbrauchs ausmacht. Ein Golf beispielsweise hat einen höheren cW-Wert von 0,37, ein Touran einen cW-Wert von 0,31. Die Überlegenheit der bionischen Form des Kofferfischs ist eigentlich kein überraschendes Ergebnis – schliesslich könnte man die Evolution des Kofferfischs als einen 1000 Jahre dauernden Funktions- und Designtest betrachten.

Die Firma Velcro des Bionik-Pioniers George de Mestral ist übrigens nach eigenen Angaben immer noch Marktführerin bei Klettverschlüssen. Nur das Einsatzgebiet hat sich seit den 1950ern erweitert: Auch in Spaceshuttles und Raumstationen wird inzwischen alles festgeklettet, damit es nicht herumschwebt.

Muskeln und Fische bringen Firmen auf neue Ideen für ihre Produkte.

5 Publications

5.1 Book chapters

1. T. Leitz, S. Ober-Blöbaum, and S. Leyendecker. *Variational Lie group formulation of geometrically exact beam dynamics: synchronous and asynchronous integration.* Computational Methods in Applied Sciences, Z. Terze (ed), Vol. 35, pp. 175-203, Springer, 2014.

2. M. Dellnitz, and M. Ringkamp. *Hierarchical Multiobjective Optimization.* Lecture Notes in Mechanical Engineering, Design Methodology for Intelligent Technical Systems, J. Gausemeier, F.J. Rammig, and W. Schäfer (eds.), Springer, DOI 10.1007/978-3-642-45435-6, 2014.

5.2 Reviewed journal publications

1. F. Demoures, F. Gay-Balmaz, S. Leyendecker, S. Ober-Blöbaum, T.S. Ratiu, and Y. Weinand. *Discrete variational Lie group formulation of geometrically exact beam dynamics.* Numerische Mathematik, DOI 10.1007/s00211-014-0659-4, 2014.

2. G. Johnson, M. Ortiz, and S. Leyendecker. *Discontinuous variational time integrators for complex multibody collisions.* Int. J. Numer. Meth. Engng., DOI 10.1002/nme.4764, Vol. 100, pp. 871-913, 2014.

3. M. Schulze, S. Dietz, B. Burgermeister, A. Tuganov, H. Lang, J. Linn, and M. Arnold. *Integration of nonlinear models of flexible body deformation in multibody system dynamics.* Journal of Computational and Nonlinear Dynamics, Vol. 9, DOI 10.1115/1.4025279, 2014.

5.3 Reviewed proceeding publications

1. T. Gail, S. Leyendecker, and S. Ober-Blöbaum. *On the role of quadrature rules and system dimensions in variational multirate integrators.* In Proceedings of the 3rd Joint International Conference on Multibody System Dynamics IMSD, USB, Busan, Korea, 30 June - 3 July 2014.

2. T. Schlögl, S. Leyendecker, S. Reitelshöfer, M. Landgraf, I.S. Yoo, and J. Franke. *On modelling and simulation of dielectric elastomer actuators via electrostatic-elastodynamic coupling.* In Proceedings of the 3rd Joint International Conference on Multibody System Dynamics IMSD, USB, Busan, Korea, 30 June - 3 July 2014.

3. T. Leitz, S. Ober-Blöbaum, and S. Leyendecker. *Variational integrators for dynamical systems with rotational degrees of freedom.* In Proceedings of WCCM XI - ECCM V - ECFD VI, Barcelona, Spain, 20-25 July 2014.

4. O.T. Kosmas, and S. Leyendecker. *Stability analysis of high order phase fitted variational integrators.* In Proceedings of WCCM XI - ECCM V - ECFD VI, Barcelona, Spain, 20-25 July 2014.

5. O.T. Kosmas, and S. Leyendecker. *Family of higher order exponential integrators.* In Proceedings of the International Conference on Mathematical Modeling in Physical Sciences, Madrid, Spain, 28-31 August 2014.

5.4 Talks

1. T. Gail, S. Leyendecker, and S. Ober-Blöbaum. *Limitations of computing time savings in variational multirate schemes.* GAMM Annual Meeting, Erlangen, Germany, 10-14 March 2014.

2. M. Koch, and S. Leyendecker. *A structure preserving approach to the simulation of non-smooth dynamics.* GAMM Annual Meeting, Erlangen, Germany, 10-14 March 2014.

3. O.T. Kosmas, and S. Leyendecker. *Stability analysis of phase fitted variational integrators.* GAMM Annual Meeting, Erlangen, Germany, 10-14 March 2014.

4. H. Lang, J. Linn, and S. Leyendecker. *Complex modal analysis for linear beams with Kelvin-Voigt material.* GAMM Annual Meeting, Erlangen, Germany, 10-14 March 2014.

5. T. Leitz, and S. Leyendecker. *Simulating underactuated multibody dynamics using servo constraints and variational integrators.* GAMM Annual Meeting, Erlangen, Germany, 10-14 March 2014.

6. M. Ringkamp, S. Ober-Blöbaum, and S. Leyendecker. *Discrete mechanics and mixed integer optimal control of dynamical systems.* GAMM Annual Meeting, Erlangen, Germany, 10-14 March 2014.

7. T. Schlögl, and S. Leyendecker. *Variational formulation and finite element modelling of electrostatic-elastodynamic coupling.* GAMM Annual Meeting, Erlangen, Germany, 10-14 March 2014.

8. T. Schlögl, and S. Leyendecker. *Electrostatic-elastodynamic finite element modelling of stacked dielectric actuators.* EuroEAP Conference, Poster, Linköping, Sweden, 10-11 June, 2014.

9. T. Gail, S. Leyendecker, and S. Ober-Blöbaum. *On the role of quadrature rules and system dimensions in variational multirate integrators.* The 3rd Joint International Conference on Multibody System Dynamics IMSD, USB, Busan, Korea, 30 June - 3 July 2014.

10. T. Leitz, S. Ober-Blöbaum, and S. Leyendecker. *Variational integrators for dynamical systems with rotational degrees of freedom.* WCCM XI - ECCM V - ECFD VI, Barcelona, Spain, 20-25 July 2014.

11. S. Leyendecker, M. Koch, M. Ringkamp, and S. Ober-Blöbaum. *A discrete variational approach to non-smooth dynamics and optimal control.* WCCM XI - ECCM V - ECFD VI, Barcelona, Spain, 20-25 July 2014.

12. O.T. Kosmas, and S. Leyendecker. *Stability analysis of high order phase fitted variational integrators.* WCCM XI - ECCM V - ECFD VI, Barcelona, Spain, 20-25 July 2014.

13. O.T. Kosmas, and S. Leyendecker. *Family of higher order exponential integrators.* International Conference on Mathematical Modeling in Physical Sciences, Madrid, Spain, 28-31 August 2014.

14. S. Leyendecker. *A discrete variational approach to hybrid dynamical systems and optimal control.* Invited lecture, IWR Research Group Optimization in Robotics and Biomechanics, Ruprecht-Karls-Universität Heidelberg, Heidelberg, Germany, 16 October 2014.

15. D. Budday, S. Leyendecker, and H. van den Bedem. *Characterizing rigidity in biomolecules with geometric tools.* Poster, BaMBA 9, Davis, California, 22 November 2014.

16. S. Leyendecker, M. Koch, M. Ringkamp, and S. Ober-Blöbaum. *Structure preserving integration of hybrid dynamical systems and optimal control.* Foundations of Computational Mathematics, Montevideo, Uruguay, 11-20 December 2014.

6 Social events

PhD defense Ramona Maas 13.01.2014

Car crash into new building

Berg 2014

Summer excursion to climbing park and devil's cave

Nikolaus hike

Christmas party 2014 together with LTM